Article
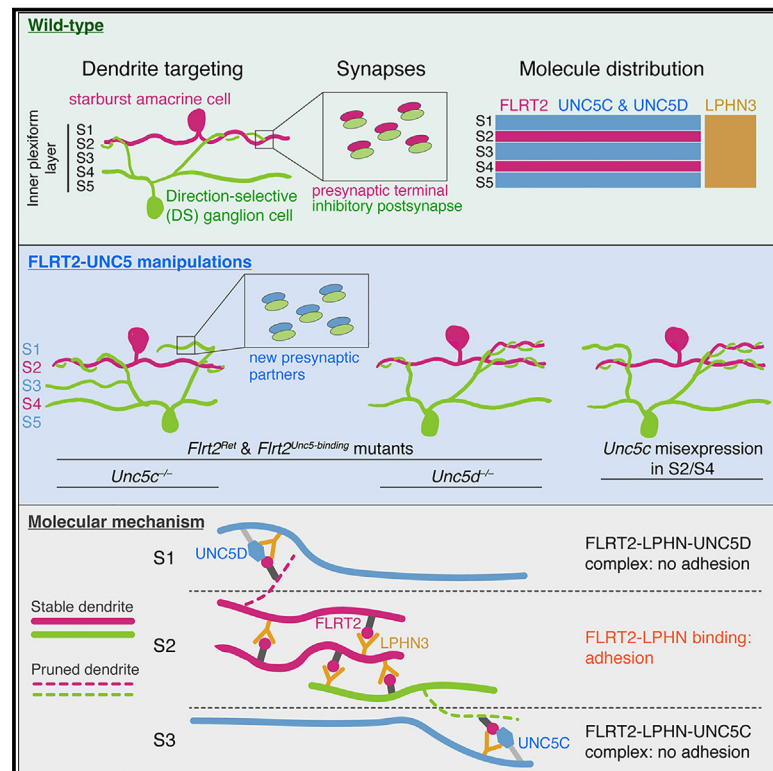
Rejection of inappropriate synaptic partners in mouse retina mediated by transcellular FLRT2-UNC5 signaling

Graphical abstract

Authors

Cameron L. Prigge, Mayur Dembla, Arsha Sharma, ..., Luca Della Santina, Marla B. Feller, Jeremy N. Kay

Correspondence

jeremy.kay@duke.edu

In brief

Precise assembly of neural circuits depends on the ability of developing neurons to shun inappropriate synaptic partners. Prigge et al. show that transcellular binding between FLRT2 and its UNC5-family ligands prevents FLRT2^{+} dendrites from adhering to inappropriate partners, thereby enforcing precise wiring of a retinal motion-sensitive circuit.

Highlights

- Retinal dendrites expressing FLRT2 and UNC5C exhibit mutual avoidance

- FLRT2-UNC5 binding promotes elimination of mistargeted dendrite branches

- Mistargeted dendrites form inappropriate synapses when FLRT2-UNC5 binding is lost

- UNC5 binding sculpts FLRT2^{+} dendrites by occluding FLRT2-latrophilin adhesion

CellPress

Article

Rejection of inappropriate synaptic partners in mouse retina mediated by transcellular FLRT2-UNC5 signaling

Cameron L. Prigge,[1,5] Mayur Dembla,[1,4] Arsha Sharma,[1,4] Malak El-Quessny,[2] Christopher Kozlowski,[1] Caitlin E. Paisley,[1] Adam M. Miltner,[1] Tyler M. Johnson,[1] Luca Della Santina,[3] Marla B. Feller,[2] and Jeremy N. Kay[1,6,*]

[1]Departments of Neurobiology, Ophthalmology, and Cell Biology, Duke University School of Medicine, Box 3802, Durham, NC 27710, USA
[2]Helen Wills Neuroscience Institute and Department of Molecular and Cell Biology, University of California, Berkeley, Berkeley, CA 94720, USA
[3]Department of Vision Sciences, University of Houston College of Optometry, Houston, TX 77204, USA
[4]These authors contributed equally
[5]Present address: Department of Physiology, Neuroscience Program, Michigan State University, East Lansing, MI 48824, USA
[6]Lead contact
*Correspondence: jeremy.kay@duke.edu
https://doi.org/10.1016/j.devcel.2023.07.011

SUMMARY

During nervous system development, neurons choose synaptic partners with remarkable specificity; however, the cell-cell recognition mechanisms governing rejection of inappropriate partners remain enigmatic. Here, we show that mouse retinal neurons avoid inappropriate partners by using the FLRT2-uncoordinated-5 (UNC5) receptor-ligand system. Within the inner plexiform layer (IPL), FLRT2 is expressed by direction-selective (DS) circuit neurons, whereas UNC5C/D are expressed by non-DS neurons projecting to adjacent IPL sublayers. *In vivo* gain- and loss-of-function experiments demonstrate that FLRT2-UNC5 binding eliminates growing DS dendrites that have strayed from the DS circuit IPL sublayers. Abrogation of FLRT2-UNC5 binding allows mistargeted arbors to persist, elaborate, and acquire synapses from inappropriate partners. Conversely, UNC5C misexpression within DS circuit sublayers inhibits dendrite growth and drives arbors into adjacent sublayers. Mechanistically, UNC5s promote dendrite elimination by interfering with FLRT2-mediated adhesion. Based on their broad expression, FLRT-UNC5 recognition is poised to exert widespread effects upon synaptic partner choices across the nervous system.

INTRODUCTION

During nervous system development, growing neurons actively choose which cells to connect with and which to avoid using cell-surface receptors. These synaptic choices establish neural circuits dedicated to specific computations and functions. Synaptogenic defects can compromise circuit function, but despite their importance, the molecular mechanisms underlying synaptic partner choices remain enigmatic.[1]

Molecular studies of synaptic specificity have mainly focused on positive cues, such as attractive or adhesive recognition molecules, that affirm appropriate connections. By contrast, far less is known about negative cues, which discourage inappropriate connections.[1–3] It is generally presumed that negative cues have important roles in wiring specificity, but few clear-cut examples are currently known.[4] Most negative cues identified so far are repulsive guidance molecules that prevent axons and dendrites from growing into particular regions.[1,3,5–7] In many cases, deletion of such guidance molecules can alter neurite targeting without disturbing the correct pairing of synaptic

partners.[8,9] Therefore, negative cues that are centrally involved in partner selection remain to be discovered.

The mouse retina is a useful model system to investigate synaptic partner choice, due to the stereotyped laminar organization of synapses within the inner plexiform layer (IPL; Figure 1A). This laminar organization facilitates the cellular rendezvous necessary for circuit-specific wiring. To examine how negative cues establish laminar and synaptic specificity, we used the mouse retinal direction-selective (DS) circuit (Figure 1A) as our model system. This evolutionarily conserved circuit encodes the direction of image motion through spiking activity of DS retinal ganglion cells (DSGCs), thereby driving multiple visual behaviors.[12–18] The DS circuit occupies two dedicated IPL sublayers, denoted S2 and S4, which respectively encode light OFF or ON responses (Figure 1A). Within these sublayers, dendrites of ON-OFF (oo)DSGCs receive input from presynaptic circuit partners, including (1) glutamatergic bipolar cells and (2) starburst amacrine cells, which provide extensive GABAergic inhibitory inputs that are a crucial determinant of the DS computation.[14,19–22] Strict dendritic co-stratification within S2 and S4 (Figure 1A)
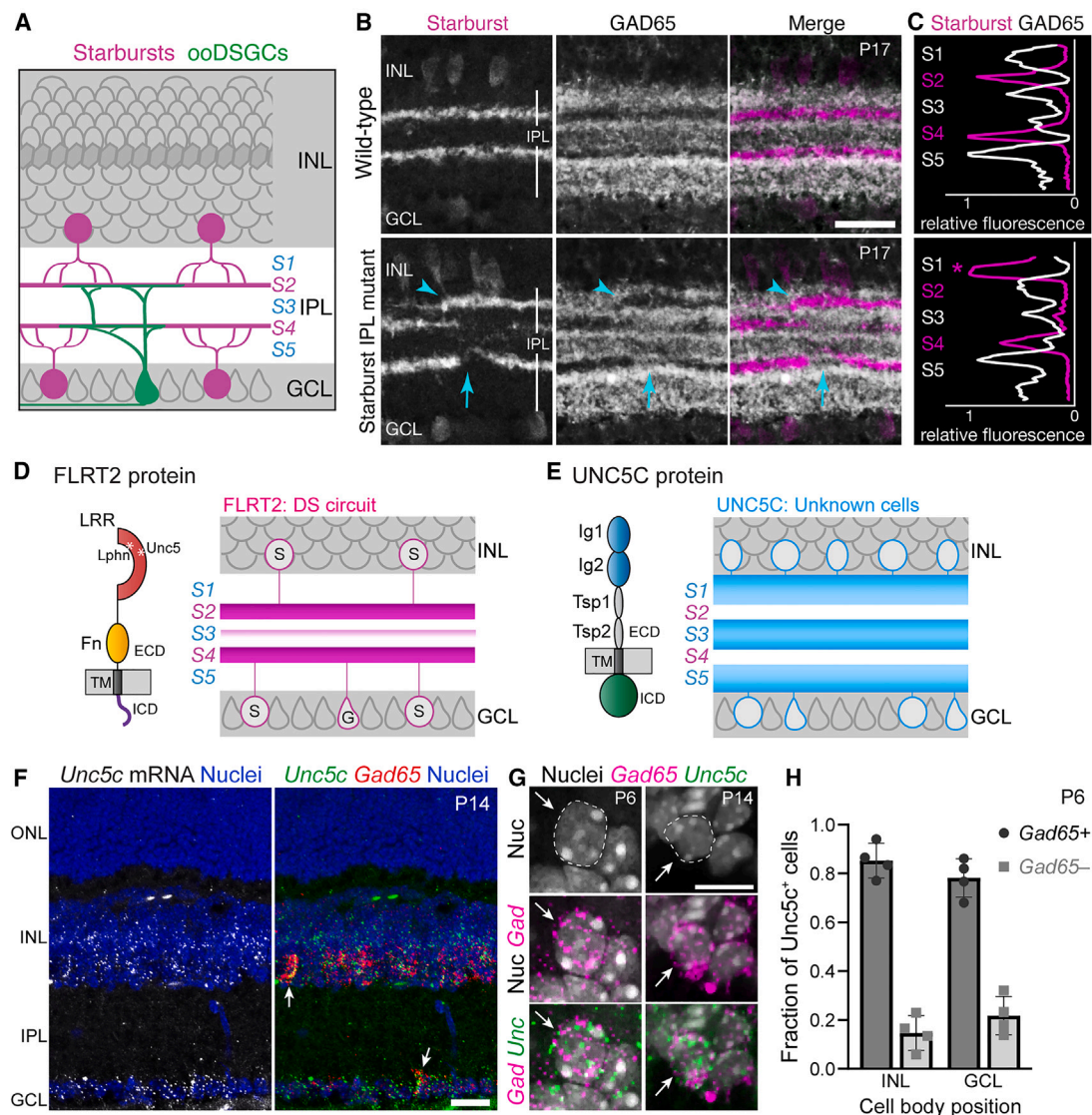
Figure 1. GAD65+ amacrine cells express UNC5C and exhibit mutual exclusion with DS circuit dendrites

(A) Schematic of mouse retina (cross-section view) showing DS circuit cell types studied here. OFF starburst amacrine cells in inner nuclear layer (INL) project to inner plexiform layer (IPL) sublayer S2; ON starbursts in ganglion cell layer (GCL) project to S4. ON-OFF direction-selective ganglion cell (ooDSGC) dendrites cofasciculate with starburst dendrites in both sublayers. Amacrine cell dendrites contain both pre- and post-synaptic sites; starburst cells release GABA and acetylcholine onto ooDSGCs.

(B and C) Perturbation of starburst dendritic targeting using *Megf10* mutants[10] reveals mutual repulsion with GAD65+ amacrine cell dendrites. (B) Retinal cross-sections stained with anti-ChAT (starburst marker) and anti-GAD65. (C) Representative profile plots quantifying ChAT and GAD65 fluorescence across IPL. Controls (top; *Megf10*^flox/flox^; no Cre, n = 4) exhibit sharp boundaries between ChAT+ and GAD65+ IPL strata. In mutants (bottom, n = 4, *Six3-Cre; Megf10*^flox/flox^), starburst dendrites enter GAD65+ IPL regions, displacing GAD65 arbors (B, arrowheads; C, asterisk). Starburst dendrites also sporadically fail to innervate regions within S2 and S4; GAD65+ arbors invade these regions (arrows).

(D and E) Schematics of FLRT2 and UNC5C protein structure (left panels) and protein localization within IPL as per our previous study[11] (right panels). FLRT2 is present in S2/S4 due to expression by ooDSGCs (G) and starburst cells (S). FLRT2 also localizes to S3. UNC5C is absent from S2 and S4 (E). LRR, leucine-rich repeat; Fn, Fibronectin-like domain; TM, transmembrane domain; ECD, extracellular domain; ICD, intracellular domain; Ig, immunoglobulin; Tsp, thrombospondin domains. FLRT2 binding sites for latrophilins (LPHNs) and UNC5s are indicated.

(F and G) *In situ* hybridization for *Unc5c* and Gad65 (gene symbol *Gad2*) to mark GABAergic amacrine cells. Blue, Hoechst nuclear counterstain. (F) Prominent *Unc5c* expression at P15 in GCL and INL, including amacrine subregion of INL (marked by Gad65). *Unc5c* labels a subset of Gad65+ amacrine cells in the INL and displaced Gad65+ amacrine cells in GCL (arrows). RGCs (Gad65-negative GCL cells) also express *Unc5c*. Expression is similar at P6 (Figure S1A). (G) Representative images of Gad65+*Unc5c*+ double-positive cells.

(H) Fraction of *Unc5c*+ cells co-expressing Gad65, quantified from images similar to (F) and (G). Most *Unc5*+ cells in GCL are GABAergic displaced amacrines rather than RGCs. n = 4 animals. Error bars, SEM.

Scale bars: 10 μm in (B) and (G) and 20 μm in (F).

Also see Figure S1.

ensures that the vast majority of inhibitory inputs onto ON-OFF direction-selective ganglion cell (ooDSGC) dendrites are supplied by starburst amacrine cells.[23–26] Numerous other amacrine cell types project to IPL sublayers directly adjacent to the DS circuit, mere microns away, and would therefore be easily accessible to ooDSGC dendrites during synaptogenesis. Nevertheless, ooDSGCs avoid such connections. The mechanisms that prevent ooDSGCs from forming synapses in adjacent non-DS layers remain unknown.

Previous studies of DS circuit synaptic specificity identified positive cues that bring DS circuit partners together within the IPL. This process starts around post-natal day (P) 0 in mice, when starbursts use homotypic recognition mechanisms to stratify their arbors into two IPL sublayers.[10,27] Then, between P0 and P6, adhesion molecules recruit ooDSGC dendrites and bipolar cell axons to the starburst laminar scaffold.[28–30] In principle, these affirmative cues could suffice to dictate laminar and synaptic specificity. However, our past work suggests that negative cues may also be positioned to drive specificity by preventing DS circuit arbors from entering adjacent non-DS sublayers.[11] We studied fibronectin leucine-rich repeat transmembrane (FLRT) proteins, a multifunctional family of cell-surface molecules that participate in adhesion, repulsion, and synaptogenesis.[31] These effects are mediated by binding to multiple ligands, including those of the uncoordinated-5 (UNC5) family.[11,32–35] We previously showed that FLRT2 and UNC5C are a repulsive receptor-ligand pair that is expressed in complementary patterns within the developing IPL. FLRT2 is expressed by starburst and ooDSGC neurons and localizes to DS circuit IPL sublayers; UNC5C, meanwhile, fills surrounding IPL strata[11] (see schematic, Figures 1D and 1E). Another FLRT2 ligand, UNC5D, shares a similar expression pattern with UNC5C.[11] In stripe assays using cultured primary retinal neurons, UNC5C inhibits arbor growth by FLRT2+ cells, including starburst amacrine cells and ooDSGCs.[11] These results suggest that FLRT2-UNC5 interactions could prevent starburst and ooDSGC dendrites from straying into adjacent IPL regions, although this idea remains to be tested in vivo.

In this study, we sought to answer two major questions. First, does FLRT2-UNC5 signaling impact DS circuit laminar specificity in vivo? We addressed this issue by focusing on DS circuit cell types that express FLRT2—the starburst amacrine cells and ooDSGCs[11]—which we refer to collectively here as "DS circuit neurons." Second, we asked how FLRT2-UNC5 signaling repels growing dendrites. We previously proposed a bidirectional "repellent receptor" model for laminar segregation, whereby FLRT2 and UNC5C both transduce repulsive guidance signals within their respective cell types upon binding to each other.[11] However, an alternative molecular model has since emerged from studies showing that FLRT2 has another key family of ligands, the latrophilins (LPHNs), and that FLRTs can simultaneously bind both ligands to form a tripartite complex.[32,34,36–38] FLRT-LPHN binding mediates adhesive and synaptogenic functions[34,39,40]; by contrast, the role of UNC5s in this complex remains uncertain. One study proposed that UNC5 binding interferes with FLRT-LPHN adhesion.[32] If this is true, UNC5s could control laminar targeting of FLRT2+ neurons by inhibiting their adhesion to LPHN substrates. Therefore, we aimed to determine whether UNC5C guides FLRT2+ arbors by a repellent receptor

mechanism, as originally proposed,[11] or by diminishing FLRT-mediated adhesion.

To address these questions, we have deployed a wide range of mouse genetic tools to selectively disrupt FLRT2-UNC5 binding. We find that the FLRT2-UNC5 system enforces DS circuit laminar and synaptic specificity in vivo. Unexpectedly, this system serves as an error-correction mechanism during a previously unappreciated developmental epoch when arbors of DS circuit neurons stray from the starburst scaffold. Finally, we show that UNC5 binding constrains growth of exuberant FLRT2+ arbors by interfering with FLRT2-LPHN adhesion. Altogether, our results support a model in which affirmative mechanisms control the initial pairing of ooDSGC and starburst dendrites, whereas negative mechanisms—mediated by FLRT2-UNC5 binding—act during subsequent dendrite growth to prevent ooDSGC arbors from abandoning their synaptic partners.
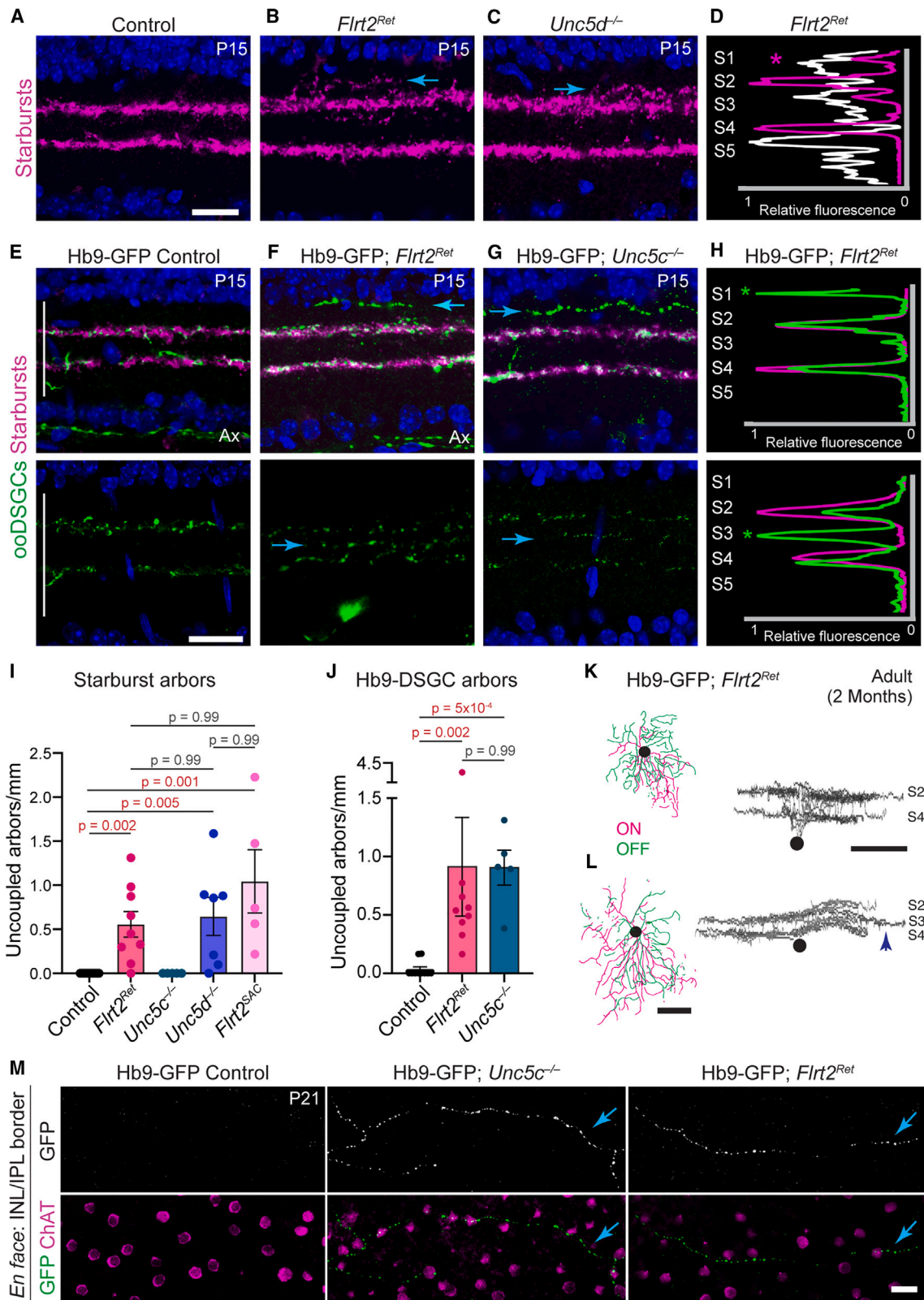
RESULTS

Repulsion between adjacent circuits establishes DS circuit-specific IPL territories

The IPL expression patterns of FLRT2 and UNC5C proteins (Figures 1D and 1E) led us to hypothesize that repulsion occurs between FLRT2+ DS circuit arbors and UNC5C+ arbors within adjacent sublayers. If this is true, there must exist a population of UNC5C-expressing neurons that exhibits mutual repulsion with the DS circuit. To identify such neurons, we focused on the amacrine subtype marked by expression of glutamic acid decarboxylase-65 (GAD65). This amacrine population, which does not include starburst cells[41] (Figure S1F), drew our attention because of the mutually exclusive IPL labeling pattern we observed in tissue double-stained for GAD65 and starburst dendrite markers (vesicular acetylcholine transporter [VAChT] or choline acetyltransferase [ChAT]; Figure 1B). These sharp boundaries suggested that repulsion may occur between DS circuit and GAD65+ arbors.

To test whether repulsion in fact occurs, we altered DS circuit laminar targeting and evaluated the effects upon GAD65+ IPL projections. To this end we leveraged a mouse mutant that perturbs laminar targeting of starburst neurons in a cell-autonomous fashion. We previously showed that Megf10 mutants exhibit focal disruptions in starburst and ooDSGC laminar targeting involving both gaps in IPL innervation and displacement of arbors into ectopic sublayers.[10] If DS circuit and GAD65+ arbors repel each other, shifting the IPL location of DS circuit arbors should produce corresponding changes in GAD65 arbors. Consistent with this prediction, mistargeted starburst arbors that entered GAD65 territory did not commingle with GAD65+ arbors, instead displacing them from their IPL strata (Figures 1B and 1C). Furthermore, gaps in DS circuit IPL sublayers were inappropriately innervated by GAD65+ arbors, suggesting a defect in repulsion when starburst and/or ooDSGC arbors are absent (Figures 1B and 1C). All mutants analyzed (n = 4) showed both types of GAD65 projection errors. These results indicate that repulsive cues prevent DS circuit and GAD65+ IPL sublayers from intermingling.

To investigate whether UNC5C could be involved in this repulsion, we next tested for expression of UNC5C by GAD65+ amacrine cells. In situ hybridization for Unc5c and Gad2—the gene

encoding GAD65—revealed that *Unc5c* labels a subset of Gad65$^+$ amacrine cells at P6 and P15 (Figures 1F, 1G, and S1A). While *Unc5c* also labeled other cell types, such as retinal ganglion cells (RGCs), most *Unc5c*$^+$ amacrine cells were Gad65$^+$ (Figures 1F–1H and S1). This finding is consistent with the notable laminar overlap between GAD65$^+$ and UNC5C$^+$ arbors in the IPL (Figures 1B and 1E). We confirmed the Gad65$^+$ identity of *Unc5c*$^+$ amacrine cells using single-cell RNA sequencing data[42] and by immunostaining primary retinal neurons in culture (n = 19/19 UNC5C$^+$ cells expressed GAD65; Figures S1B–S1E). Altogether, these results demonstrate that UNC5C is expressed by a specific GABAergic amacrine subpopulation that exhibits mutual repulsion with FLRT2$^+$ DS circuit IPL arbors. Therefore, this receptor-ligand pair is positioned to provide repulsive laminar targeting cues during DS circuit development.

DS circuit laminar targeting errors in *Flrt2* mutant mice

To test whether FLRT2-UNC5C signaling is required for DS circuit laminar targeting, we used a variety of genetic approaches to disrupt this interaction and then assessed whether starburst or ooDSGC dendritic arbors stray from their normal S2 and S4 sublayers. First, we generated retina-specific *Flrt2* mutants (denoted *Flrt2*^{Ret}), in which *Six3-Cre*[43] drives retinal recombination of a *Flrt2*^{flox} allele. Antibody labeling verified that FLRT2 protein was absent from retinas of *Flrt2*^{Ret} mice (Figure S2). Laminar targeting phenotypes were assessed in mutants and wild-type littermates (*Flrt2*^{WT}) at P15–P17.

We first examined starburst arbors in *Flrt2*^{Ret} mutants. A sporadic laminar targeting phenotype was observed in mutant retina, whereby starburst neurons intermittently misprojected primarily into the S1 IPL sublayer (Figure 2B, 2D, and 2I). By contrast, *Flrt2*^{WT} starburst projections were confined to S2 and S4 (Figures 2A, 2I, and S3A–S3D). A similar phenotype was observed when *Flrt2* was deleted using the starburst-specific *Chat*^{Cre} mouse, indicating that FLRT2 is functioning within starburst cells (Figures 2I and S3A–S3D). To ascertain whether starburst laminar targeting errors could involve defects in cross-circuit repulsion, we cultured primary neurons from neonatal retina and measured the overlap between starburst and GAD65$^+$ neurites. Overlap was significantly greater in *Flrt2*^{Ret} cultures compared with *Flrt2*^{WT} control cultures, suggesting a defect in cell-cell avoidance when FLRT2 is absent (Figures S3E and S3F).

We next examined ooDSGC laminar targeting in *Flrt2*^{Ret} mutants. To this end we used the *Hb9-GFP* transgene, which selectively marks ooDSGCs (Figures S4A and S4B) that prefer ventral motion.[44] Two types of ooDSGC laminar targeting alterations were observed in *Flrt2*^{Ret} animals, each of which occurred sporadically across mutant retina. First, wherever starburst arbors were mistargeted, ooDSGC dendrites remained aligned with them (Figure S3G), consistent with our past findings that ooDSGCs always follow starburst laminar errors.[10] Because ooDSGCs remained correctly paired with starbursts in these instances, they were scored as starburst errors rather than ooDSGC errors.

However, we also observed a second type of error—scored as ooDSGC errors—in which Hb9-DSGC dendrites became sporadically uncoupled from their starburst partners. In these cases, ooDSGC dendrites stratified within ectopic IPL regions that did not contain starburst arbors (Figures 2E, 2F, 2H, and 2J). These laminar errors were highly specific: when not associated with the starburst scaffold, Hb9-DSGC dendrites instead targeted stereotyped ectopic locations in S1 and S3 (Figures 2F, 2H, and 2L). Some ectopic projections extended over large distances in a minimally branched manner (Figure 2M)—a growth pattern that differs substantially from the highly branched arbors in S2 or S4 (Figures 2K and 2L). Therefore, ectopic arbors appear to represent a new dendritic growth pattern that is appended onto the normal arbor. We also observed ooDSGC laminar errors in *Six3-Cre; Flrt2*$^{flox/+}$ heterozygotes, albeit at lower frequency (Figures S4C and S4D). Ectopic arbors did not co-label with the axon marker Neurofilament-M, confirming their dendritic identity (Figure S4E). Single-cell reconstructions revealed that ~25% of *Flrt2* mutant Hb9-DSGCs made dendritic laminar errors (Figures 2K and 2L, n = 3/12 cells projected ectopically). By contrast, *Flrt2*^{WT} control animals rarely exhibited Hb9-DSGC dendrites outside the sublayers defined by starburst arbors (Figures 2E and 2J). Loss of *Flrt2* also disrupted laminar targeting of a second ooDSGC subtype, marked by the *Drd4-GFP* transgene[45,46] (Figures S5A and 5B). Altogether, these *Flrt2*^{Ret} phenotypes indicate that FLRT2 influences precise laminar targeting by both starburst cells and ooDSGCs.

Figure 2. Starburst and ooDSGC laminar targeting errors in *Flrt2* and *Unc5* mutants

(A–D) Starburst dendrite targeting errors in *Flrt2*^{Ret} and *Unc5d* mutants.

(A–C) Representative cross-section images; (D), fluorescence profile plots (white, anti-GAD65). Magenta, anti-VAChT. Arrows (A–C) and asterisks (D) mark ectopic starburst dendrites in S1.

(E–H) Hb9-ooDSGC dendrite targeting errors in *Flrt2*^{Ret} and *Unc5c* mutants. Magenta, anti-VAChT; green, anti-GFP (labeling ooDSGCs). Vertical bar, IPL neuropil. Arrows (E–G) and asterisks (H) mark ectopic ooDSGC arbors in S1 (top row) or S3 (bottom row) that are uncoupled from starburst arbors. Ax, GFP$^+$ axons within nerve fiber layer. Blue, Hoechst nuclear counterstain.

(I and J) Summary of starburst (I) and ooDSGC (J) laminar targeting errors. ooDSGC phenotype strength was similar in *Flrt2*^{Ret} and *Unc5c*$^{-/-}$. Starburst phenotype strength was similar in *Flrt2* whole-retina (*Flrt2*^{Ret}) and starburst-specific (*Flrt2*^{SAC}) mutants, as well as *Unc5d*$^{-/-}$. Statistics (I), Kruskal-Wallis test (main effect p = 1.6 × 10^{-5}) with Dunn's post hoc test. Sample sizes (number of animals): littermate controls n = 9, *Flrt2*^{Ret} n = 9, *Unc5c*$^{-/-}$ n = 5; *Unc5d*$^{-/-}$ n = 7; *Flrt2*^{SAC} n = 5. Statistics (J), Kruskal-Wallis test (main effect p = 9.2 × 10^{-5}) with Dunn's post hoc test. Sample sizes (number of animals): littermate controls n = 11 (n = 6 *Flrt2*^{WT}; n = 5 *Unc5c*$^{+/+}$), *Flrt2*^{Ret} n = 9, *Unc5c*$^{-/-}$ n = 5. p values (shown on graph) were corrected for multiple comparisons.

(K and L) Single-cell reconstructions of dye-filled Hb9-ooDSGCs from *Flrt2*^{Ret} mutants. K, normally stratified ooDSGC; L, ooDSGC with ectopic S3 dendritic arbor (arrowhead). n = 3/12 filled cells exhibited ectopic arbors.

(M) En-face view of ectopic ooDSGC arbors in retinal whole mounts. To depict S1 IPL sublayer, confocal images were acquired at plane of IPL/INL border. Hb9-GFP$^+$ arbors do not project to this location in wild-type retina (left) but are readily observed in both *Unc5c*$^{-/-}$ and *Flrt2*^{Ret} mutants (arrows).

Scale bars: 20 μm in (A)–(C), (E)–(G), and (M) and 100 μm in (K) and (L). Error bars, SEM.

Also see Figures S2–S5.

Cell-type-specific roles for *Unc5c* and *Unc5d* in DS circuit laminar targeting

As a second way of disrupting FLRT2-UNC5C signaling, we next utilized an *Unc5c* constitutive-null allele.[47,48] Because *Unc5c*^{−/−} animals on a pure C57BL/6J background rarely survived beyond P0, these experiments used a hybrid C57-SJL background (see STAR Methods). Whereas mistargeted Hb9-DSGC arbors were rare in *Unc5c*^{+/+} control retinas, we found numerous ooDSGC errors in *Unc5c*^{−/−} mutants (Figures 2G and 2J). *Unc5c*^{−/−} errors strikingly resembled those observed in *Flrt2*[Ret] animals and occurred at similar frequency in each mutant, strongly suggesting that each mutation is affecting the same underlying molecular event (Figures 2E–2H, 2J, 2M, and S5C). These findings support the notion that UNC5C prevents mistargeting of ooDSGC arbors via transcellular interactions with FLRT2.

In contrast to ooDSGCs, starburst IPL projections were entirely normal in *Unc5c*^{−/−} mutants (Figure 2I). We therefore considered whether a different FLRT2 binding partner might influence starburst laminar restriction. UNC5D is a close homolog of UNC5C that also binds FLRT2, and which also localizes to non-DS IPL regions in a pattern resembling UNC5C.[11] Furthermore, similar to *Unc5c*, *Unc5d* is broadly expressed by GAD65+ GABAergic amacrine cells (Figures S1C–S1E). These findings prompted us to examine DS circuit IPL targeting in *Unc5d*^{−/−} mutant mice.[35] We observed a starburst IPL phenotype in *Unc5d* mutants that was notably similar to the *Flrt2*[Ret] phenotype (Figures 2C, 2I, and S3A–S3D). By contrast, Hb9-DSGC dendrite targeting was unaffected by loss of *Unc5d* (Figures S3H and S3I). Together, these results support a model in which UNC5D-FLRT2 signaling influences starburst laminar specificity, whereas UNC5C-FLRT2 signaling influences laminar specificity of ooDSGCs.

Direct FLRT2-UNC5 protein interactions mediate DS circuit laminar targeting

To critically test the model that DS circuit laminar targeting depends on direct FLRT2-UNC5C binding, we selectively disrupted FLRT2-UNC5 interactions *in vivo*. Structural studies have identified a FLRT ectodomain point mutation, FLRT2[H170N] (Figure 3A), that blocks UNC5 binding without altering trafficking, surface expression, or interactions with LPHNs.[33,37] This so-called FLRT2[UF] mutation has been used extensively to test functional consequences of FLRT2-UNC5 signaling.[32,33,37,38,49] Using CRISPR editing, we introduced the *Flrt2*[UF] point mutation into the mouse germline. *Flrt2*[UF/UF] animals (abbreviated *Flrt2*[UF]) on a pure C57BL/6 background showed reduced survival beyond P0. However, similar to *Unc5c*^{−/−} mice, *Flrt2*[UF] mutants did survive and appeared grossly normal when bred on a mixed C57BL/6-SJL background. Therefore, we used this mixed background to investigate retinal phenotypes at P15–P17 in *Flrt2*[UF] mice.

Flrt2[UF] mutants exhibited starburst (Figures 3B–3D) and ooDSGC (Figures 3E–3G) dendrite phenotypes that were strikingly similar to those observed in *Flrt2*[Ret], *Unc5c*^{−/−}, and/or *Unc5d*^{−/−} mutants. Comparing *Flrt2*[UF] to *Flrt2*[Ret], which completely lacks retinal *Flrt2* function, the number of starburst errors was similar (Figure 3D). Thus, loss of UNC5 binding appears to fully account for the *Flrt2* starburst phenotype. The number of ooDSGC errors was also comparable between *Flrt2*[UF] and *Flrt2*[Ret]—we did not detect a statistically significant difference

between the groups. However, we did note a trend toward fewer errors in *Flrt2*[UF], suggesting that other FLRT2 ligands may cooperate with UNC5s to mediate ooDSGC laminar targeting (Figure 3G). Nevertheless, these findings support the conclusion that UNC5s are the major FLRT2 ligands mediating suppression of mistargeted DS circuit arbors.

Mistargeted ooDSGC arbors receive non-starburst inhibitory synapses

We next investigated whether removal of FLRT2-UNC5C signaling impacts DS circuit synaptic specificity. Normally, starburst amacrine cells provide virtually all inhibitory synapses onto ooDSGC dendrites.[21,25,26,50] However, in *Flrt2*[Ret] and *Unc5c*^{−/−} mutants, ooDSGCs send dendrites into IPL regions lacking starburst arbors (Figure 2), suggesting that they might receive inhibitory synapses from inappropriate non-starburst partners. To test for inhibitory synapses on mistargeted Hb9-DSGC dendrites, we labeled synapses using antibodies to the presynaptic active zone marker bassoon and the inhibitory post-synaptic marker gephyrin (Figures 4A, 4B, S5D, and S5E). We then used Object Finder software[51] to perform unbiased semi-automated identification of paired bassoon-gephyrin synapses on Hb9-GFP+ arbors. We assessed both mutants but were particularly focused on *Unc5c*^{−/−} animals because they lack mistargeted starburst arbors (Figure 2I). Thus, in *Unc5c*^{−/−} mutants we can be certain that starburst cells are not the source of synapses onto mistargeted ooDSGC dendrites.

This analysis revealed that mistargeted Hb9-DSGC dendrites in *Unc5c* mutants were studded with putative inhibitory synapses, at a density resembling properly localized arbors within S2 and S4 (Figure 4C). Indeed, inhibitory synapses were identified on all mistargeted S1 and S3 arbors analyzed (n = 4 *Unc5c*^{−/−}, n = 4 *Flrt2*[Ret]; 2 sections per animal). These results indicate that mistargeted Hb9-DSGC dendrites receive numerous inappropriate connections from non-DS circuit inhibitory synaptic partners—probably in both mutants, but certainly in *Unc5c*^{−/−}.

Maintenance of DS circuit laminar targeting mediated by FLRT2-UNC5 repulsion

To understand the mechanism by which FLRT2-UNC5 signaling controls dendritic laminar targeting, we first sought to determine the developmental events that depend on presence of these molecules. Initial formation of the DS circuit IPL sublayers is a two-step process involving stratification of starburst arbors by P2, and ooDSGC dendrites by P6[10,29] (Figures 5A and 5B). Both of these events occurred normally in *Flrt2*[Ret] and *Unc5c*^{−/−} mutants, indicating that these genes are dispensable for initial circuit assembly (Figures 5E, 5F, and S6).

We next investigated DS circuit laminar development between P6 and P15. This period encompasses the functional maturation of the DS circuit[52–54] and is characterized by horizontal expansion of starburst and ooDSGC arbors within S2 and S4.[55–57] In wild-type retina, we noticed a previously unreported refinement of ooDSGC lamination between P6 and P15. While gross stratification of DS circuit arbors was complete by P6, we observed occasional mistargeted ooDSGC dendrites at P6 and P10 that were not paired with the starburst scaffold (Figures 5B and 5C). These mistargeted dendrites were eliminated by P15 (Figures 5D and 5E). In *Flrt2*[Ret] and *Unc5c*^{−/−} mutants, the
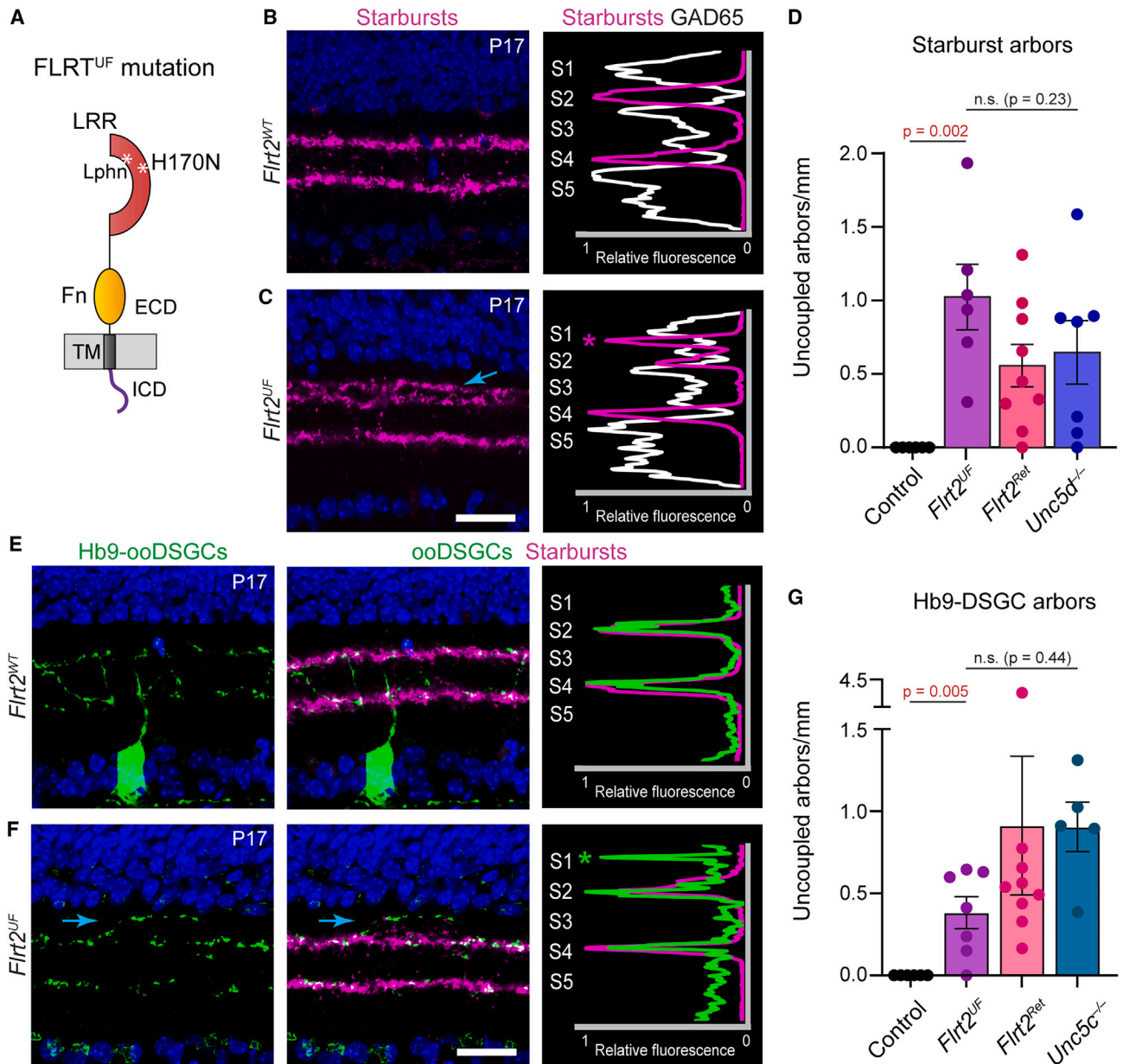
Figure 3. Abolishing FLRT2-UNC5 binding disrupts DS circuit laminar targeting

(A) FLRT2^UF^ mutant protein. H170N mutation introduces N-glycosylation site within LRR domain at UNC5 binding surface. LPHN binding site is unaffected. Abbreviations, see Figures 1D and 1E.

(B and C) Starburst laminar targeting errors in homozygous *Flrt2^UF^* mutants. Left, VAChT immunostaining; right, profile plots (VAChT and GA65 fluorescence). Unlike controls (B), mutants (C) exhibit ectopic dendrites within S1 (arrow, asterisk).

(D) Summary of starburst laminar errors in *Flrt2^UF^* mutants and *Flrt2^WT^* littermate controls. Statistics, two-tailed Mann-Whitney test; sample sizes n = 6 littermate controls; n = 6 *Flrt2^UF^* mutants. For comparison, *Flrt2^Ret^* and *Unc5d^−/−^* mutant data are replotted from Figure 2. There was no significant difference in error frequency between *Flrt2^UF^* and the other two mutants (one-way ANOVA, $F_{(2, 19)} = 1.60$; n.s., not significant).

(E and F) ooDSGC dendrite targeting errors are observed in *Flrt2^UF^* mutants (F) but not littermate controls (E). Arrow, ectopic ooDSGC arbor within S1.

(G) Summary of Hb9-ooDSGC laminar errors in *Flrt2^UF^* mutants and *Flrt2^WT^* littermate controls. Statistics, two-tailed Mann-Whitney test; sample sizes n = 6 littermate controls; n = 7 *Flrt2^UF^* mutants. For comparison, *Flrt2^Ret^* and *Unc5c^−/−^* mutant data are replotted from Figure 2. There is a trend toward fewer errors in *Flrt2^UF^* compared with the other two mutants but the difference was not significant (one-way ANOVA, $F_{(2, 18)} = 0.85$).

Scale bars, 20 μm. Error bars (D and G), SEM.

Hb9-GFP; *Flrt2^Ret*

A — Hb9-GFP

B — GFP Bassoon Gephyrin

Hb9-GFP; *Unc5c^−/−*
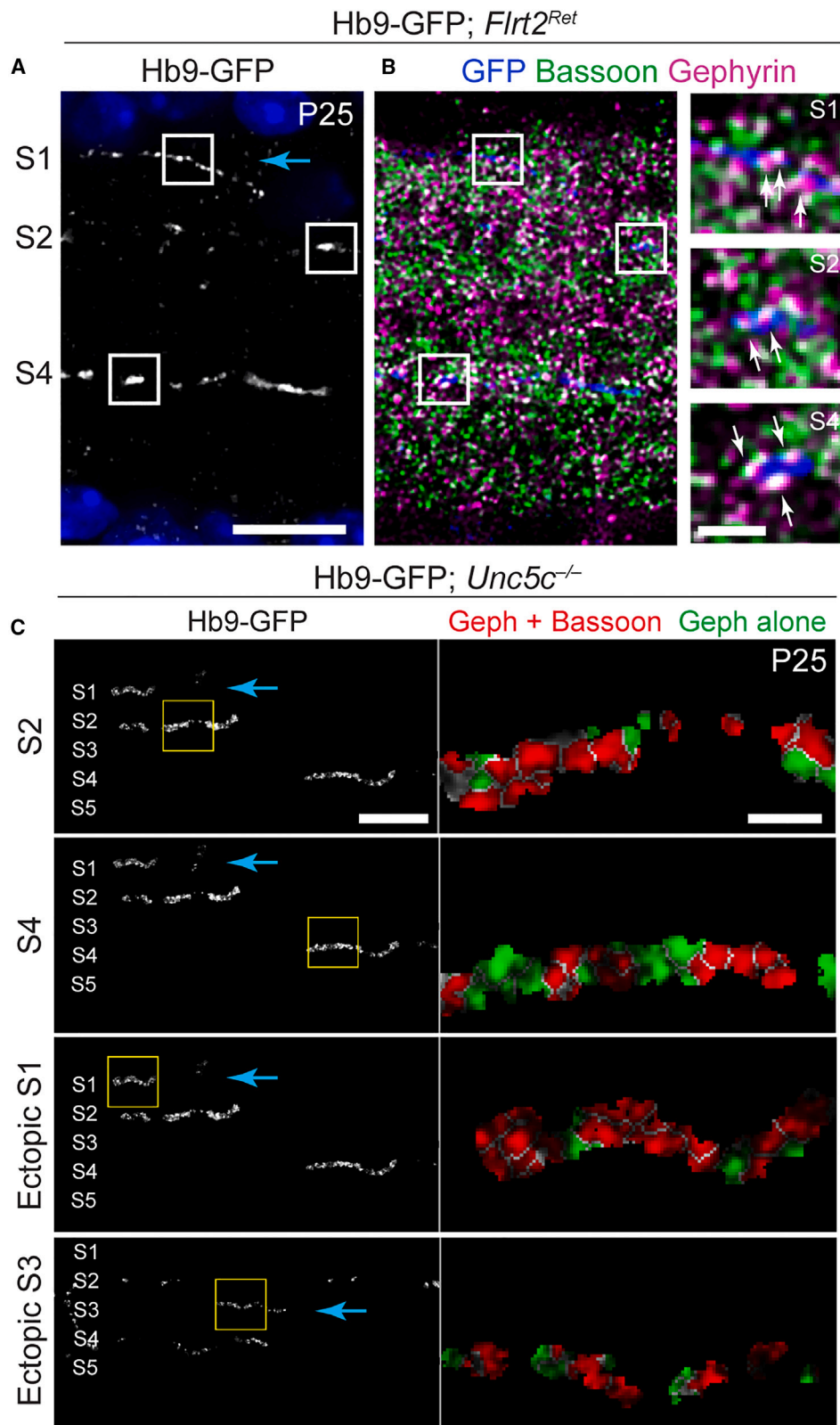
C — Hb9-GFP — Geph + Bassoon Geph alone

Figure 4. Mistargeted ooDSGC arbors in *Flrt2^Ret* and *Unc5c* mutants receive inhibitory synapses

(A and B) Inhibitory synapse labeling in P25 *Hb9-GFP*; *Flrt2^Ret* mutant (single optical slice from representative confocal stack). (A) GFP channel alone; blue arrow, ectopic ooDSGC arbor. (B) GFP overlay with bassoon and gephyrin. Boxed regions are shown at high magnification (B, right). White signals indicate putative

(legend continued on next page)

number of mistargeted ooDSGC dendrites was similar to controls at P6 and P10 (Figures 5E and S6). Subsequently however, rather than eliminating mistargeted dendrites, both mutants showed a substantial increase in mistargeting from P10 to P15 (Figure 5E). A similar phenomenon occurred for starburst arbors between P6 and P10 (Figure 5F). These findings indicate that, even after targeting the correct IPL sublayer by P6, growing DS circuit dendrites are not exclusively confined to the appropriate sublayer. Rather, they continue to produce mistargeted branches which are eliminated in a FLRT2-UNC5-dependent manner.

UNC5s influence dendrite targeting by interfering with FLRT-LPHN adhesion

We next addressed the molecular mechanisms by which FLRT2-UNC5 binding suppresses growth of mistargeted DS circuit dendrites. One straightforward possibility is that binding initiates a repulsive signal, transduced either by FLRT2 or a co-receptor,[58] that inhibits arbor growth. If this repellent receptor model (Figure 6A) is correct, FLRT2 should be required cell autonomously for repulsion. To test this model, we deleted *Flrt2* selectively from RGCs, using the Vglut2[Cre] driver. In these *Flrt2*[RGC] mutants, ooDSGCs laminar targeting was normal, indicating that FLRT2 is not required cell autonomously (Figures 6B and 6C). Thus, FLRT2 is unlikely to function within a repellent receptor complex.

An alternate model is that FLRT2-UNC5 binding prevents elaboration of mistargeted dendrites by depriving them of FLRT2-mediated positive growth signals. FLRT adhesion can generate positive cues for synapse formation via LPHN binding.[34,39] If FLRT2-LPHN adhesion occurs among starburst and ooDSGC dendrites, this could stabilize correctly targeted nascent dendrite branches within S2 and S4 (Figure 6D). Mistargeted branches, by contrast, would be subject to FLRT2-UNC5 binding, which is thought to diminish FLRT-LPHN adhesion through formation of the UNC5-FLRT-LPHN ternary complex.[32] As such, mistargeted dendrites encountering UNC5s may fail to receive FLRT2-LPHN positive signals, leading to their removal (Figure 6D).

For this "adhesion-occlusion" model (Figure 6D) to be correct, three key conditions must be met: (1) LPHNs should be expressed within developing retina and should form a ternary FLRT2-UNC5C-LPHN complex, (2) LPHNs should promote adhesion and stabilization of DS circuit dendrites, and (3) FLRT2-UNC5 binding should inhibit LPHN-mediated dendritic adhesion/stabilization. We tested each of these predictions in the following series of experiments. First, pull-down studies showed that a protein complex containing LPHN3, FLRT2, and UNC5C is indeed present in developing retina (Figure 6E). To learn which cells express LPHNs, we leveraged multiple transcriptomic datasets,[42,59–61] which were in agreement that

Lphn1 and *Lphn3* are broadly expressed by most RGCs and amacrine cells, including starburst neurons and ooDSGCs. This expression pattern suggests that LPHNs are available throughout the IPL for FLRT2 binding, in which case UNC5-mediated suppression of LPHN-FLRT2 adhesion may be critical for restricting DS circuit dendrites to their appropriate sublayers (see model, Figure 6D).

Second, to test whether LPHNs are affirmative cues for nascent DS circuit dendrites, we used an adhesion assay in which primary retinal neurons are cultured with HEK293 cells expressing cDNAs of interest.[62] VAChT immunostaining revealed that starburst arbors associated extensively with HEK cells expressing LPHN3-GFP, but not GFP alone (Figures 6F and 6G). Therefore, FLRT2^{+} starburst cells are subject to LPHN3-mediated adhesion, which is sufficient to stabilize arbors that have contacted LPHN3^{+} cells.

Third, to test whether UNC5s can interfere with starburst-LPHN3 adhesion, we performed the co-culture adhesion assay using HEK cells expressing both UNC5C and LPHN3. Remarkably, co-expression of UNC5C blocked starburst arbors from adhering to LPHN3 HEK cells (Figures 6F and 6G). This inhibitory effect depends on transcellular binding of UNC5C to starburst FLRT2, because when we instead co-expressed an UNC5C[UF] point mutant that cannot bind FLRTs,[33] starburst adhesion to LPHN3 HEK cells was restored (Figures 6F and 6G). We conclude that FLRT2-UNC5 binding inhibits FLRT2-LPHN3 adhesion and that this anti-adhesive effect suffices to influence starburst dendrite targeting. These results support a model whereby FLRT2-UNC5 binding drives elimination of mistargeted DS circuit dendrites by depriving them of FLRT-LPHN adhesion (Figure 6D).

UNC5C suppresses elaboration of DS circuit arbors to guide laminar targeting

A key prediction of the adhesion-occlusion model (Figure 6D) is that UNC5 expression within non-DS circuit IPL strata renders these regions inhospitable to DS circuit dendrite growth. To test this prediction, we misexpressed UNC5C in the DS circuit IPL sublayers. If our working model is correct, UNC5C mislocalization should impede correctly targeted DS circuit dendrites from receiving FLRT2-mediated affirmative cues, thereby diminishing growth within S2/S4 and favoring growth within ectopic sublayers (Figures 7G and 7H). To misexpress UNC5C, we generated an adeno-associated virus (AAV) construct that expresses hemagglutinin (HA)-tagged UNC5C protein in a Cre-dependent manner (AAV-CMV-flex-UNC5C-HA). This virus was introduced intravitreally at P1 or P2 into *Chat*[Cre] transgenic mice (Figure 7A), which express Cre recombinase selectively in starburst cells.[10] This AAV misexpression strategy is denoted Chat-UNC5C. Starburst-specific expression of UNC5C protein

---

synaptic sites where bassoon and gephyrin puncta overlap. Putative synapses (white arrows) are observed along ooDSGC dendrites in normal DS circuit sublayers (S2, S4) and ectopic sublayers (S1).

(C) Semi-automated unbiased synapse identification in *Hb9-GFP*; *Unc5c*^{−/−} mutant. ObjectFinder software was used to analyze images similar to (B). Left, GFP channel 3D mask, demarcating ooDSGC dendrites. Right, segmentation of paired bassoon-gephyrin synaptic structures (red) within GFP mask. Synapses are evident along ectopic arbors (S1, S3, blue arrows), similar to normally targeted arbors (S2, S4). Green, non-synaptic gephyrin signal (i.e., without bassoon co-localization). Images are representative of n = 4 *Unc5c*^{−/−} and n = 4 *Flrt2*[Ret] animals.

Scale bars: 10 μm in (A and B, left), 2 μm in (B, right), 20 μm in (C, left), and 5 μm in (D, right).
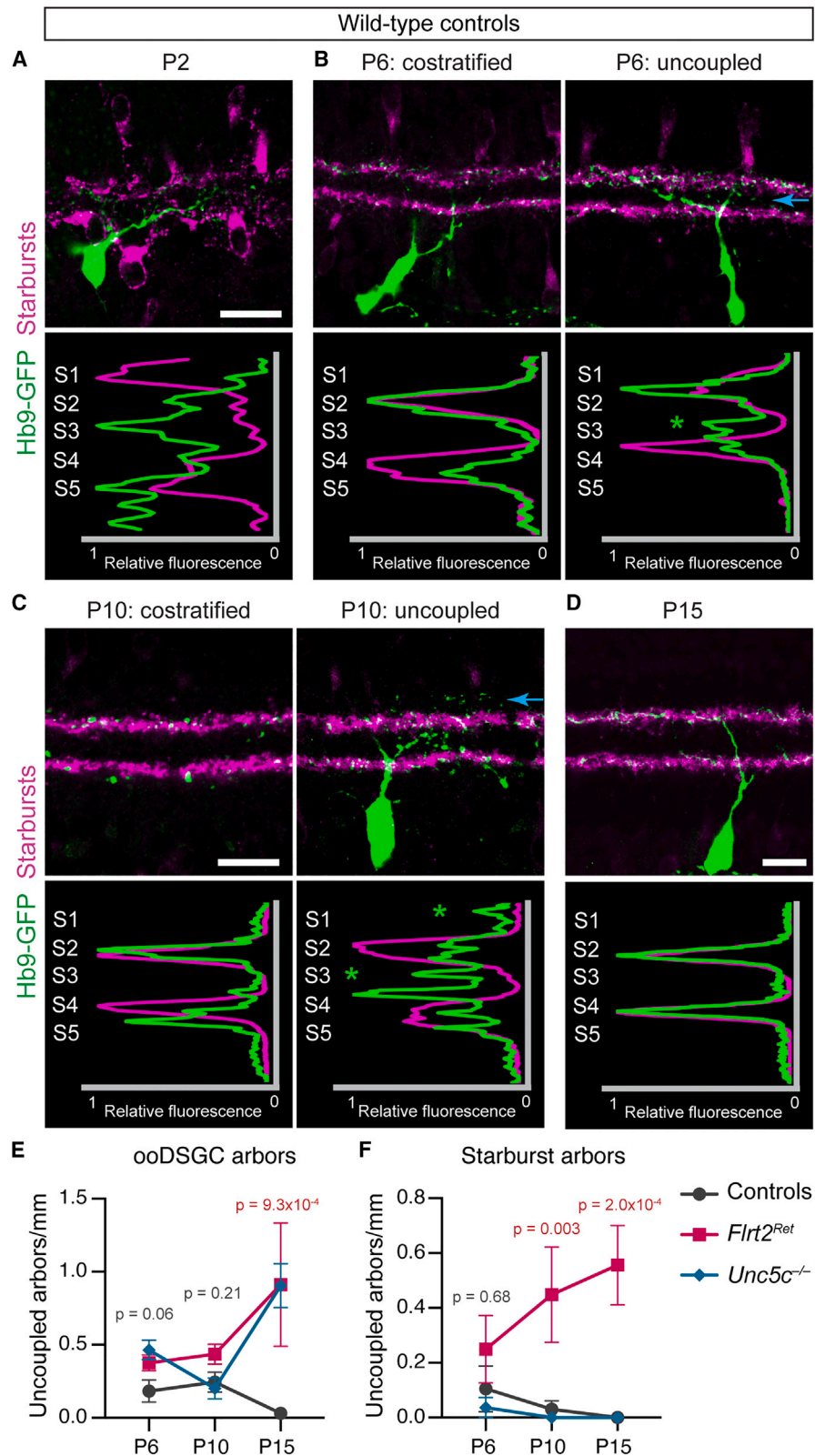
Also see Figures S5D and S5E.

Figure 5. Refinement of DS circuit laminar targeting between P6 and P15

(A–D) Developmental time course showing starburst and Hb9-ooDSGC IPL projections at specified ages. All images from wild-type animals (i.e., *Flrt2*^{+/+}; *Unc5c*^{+/+}); for mutant images, see Figure S6. At P2 (A), starburst IPL strata are evident; ooDSGC arbors are not yet stratified. At P6 (B) and P10 (C), both cell types

was validated by anti-HA immunolabeling (Figures S7B–7E). Cre-dependent flex-tdTomato AAV was used as an injection control (Figure 7A).

Compared with starburst cells expressing tdTomato alone, starbursts from retinal regions transduced with UNC5C AAV exhibited altered morphology consistent with impaired elaboration of arbors within sublayer S2 (Figures 7B, 7C, and S7A; n = 5/5 whole-mount retinas from 5 Chat-UNC5C mice). Furthermore, we observed starburst laminar targeting errors in Chat-UNC5C animals that were absent from tdTomato-only controls (Figure 7F; n = 4/4 controls without laminar errors; n = 5/5 Chat-UNC5C with errors). These errors closely resembled the starburst phenotype in *Flrt2*[Ret] and *Unc5d*^{−/−} mutants (Figure 2). We also observed mistargeting of Hb9-DSGC dendrites in Chat-UNC5C mice (n = 4/4 mice had errors; n = 0/4 Tomato-only controls had errors), indicating that starburst-derived UNC5C acts in a transcellular manner to produce ooDSGC laminar targeting errors (Figures 7D and 7E). Altogether, these results indicate that ectopic UNC5C favors elaboration of mistargeted DS circuit dendrites at the expense of correctly targeted ones, as expected if UNC5s are inhibitors of FLRT2-mediated adhesion (Figures 7G and 7H).

DISCUSSION

It has been suggested that affirmative cues may suffice to specify most synaptic partner choices: inappropriate partners may be rejected simply because they lack the correct adhesive code.[3,63] However, in this study we demonstrate that negative cues also contribute in critical ways to laminar and synaptic specificity. We show that direct binding of FLRT2 to its ligands UNC5C and UNC5D serves as an error-correction mechanism for retinal DS circuit dendrites during a period of exuberant arbor growth and refinement. When FLRT2-UNC5 transcellular signals are disrupted, ooDSGCs generate ectopic dendrites that are uncoupled from their starburst partners, instead acquiring numerous inhibitory synapses from other amacrine cells. Therefore, FLRT2-UNC5-negative signals are part of the mechanism by which ooDSGCs shun inappropriate synaptic partners. This retinal function of FLRT2-UNC5 signaling is reminiscent of how the Semaphorin-Plexin system controls synaptic specificity in Drosophila ellipsoid body and mammalian spinal cord.[4,64] In all three cases, negative cues sculpt a layered neuropil, restricting circuit-specific arbors to laminae where synaptic partners are located. Thus, our study reveals common situations requiring negative synapse specificity cues, even when these cues are encoded by highly divergent molecular families.

Our findings also highlight how negative synapse specificity cues operate in concert with positive cues. We provide evidence that FLRT2-LPHN binding is part of the adhesive system that af-

firms DS circuit contacts and that UNC5s exert their inhibitory effects by interfering with this adhesion. Thus, the FLRT-LPHN-UNC5 protein complex[32,37] may be a key molecular hub for synaptic choices, mediating positive wiring signals when UNC5s are absent from the complex but negative signals when UNC5s are present (Figure 7G). Due to their widespread expression, this FLRT-LPHN-UNC5 hub may influence synaptic partner choices not only in the retina but also elsewhere in the nervous system.

Implications for understanding FLRT-UNC5 signaling mechanisms

FLRT and UNC5 proteins are emerging as important contributors to many facets of brain development and disease.[31,65–69] Previous studies have emphasized FLRTs as ligands and UNC5s as repulsive guidance receptors.[35,49] By contrast, our results reveal that signaling in the reverse direction is also possible: we show that FLRT2-expressing dendrites can be sculpted by UNC5 binding. These findings raise the intriguing possibility that FLRT2-UNC5 binding may mediate bidirectional repulsion—a mechanism that would have obvious utility in establishing discrete IPL sublayers (Figure 1B). It will be informative to learn, in future studies, whether UNC5C- or UNC5D-expressing populations also exhibit targeting errors in *Flrt2* mutants.

Many previous studies have shown that FLRTs bind LPHNs to promote transcellular adhesion, synaptogenesis, and cell migration.[34,39,40,70] While it was known that UNC5s can form a ternary complex with LPHNs and FLRTs, the function of the complex *in vivo* remained unexplored. Our results suggest that inclusion of UNC5s within this complex inhibits FLRT-LPHN adhesion. While further work will be needed to prove this molecular model, our study establishes that UNC5s can counter FLRT-LPHN adhesion to control dendrite development and synaptic specificity *in vivo*.

Role of FLRT2-UNC5 signaling in direction-selective circuit assembly

Establishment of DS circuit IPL sublayers between P0 and P6 is driven by positive cues that pair starburst dendrites with their synaptic partners.[28–30] While prior studies presumed that starburst-ooDSGC laminar targeting was complete by P6,[29,57] we show that these neurons continue to generate transient mistargeted branches during the P6–P15 period, which are eliminated in a FLRT2-UNC5 dependent manner. Why might DS circuit dendrites stray from their laminar scaffold during this time? We favor the possibility that stray arbors are an inevitable consequence of dendrite growth. The exuberant branching period coincides with a time when starbursts and ooDSGCs grow substantially in the tangential plane of the retina: adult arbor sizes are reached by ~P14.[56,57,71] Dendrites typically grow by an iterative process in

---

are largely co-stratified although uncoupled ooDSGC arbors outside S2/S4 are evident (right panels; arrows). By P15 (D) all ooDSGC dendrites are coupled with starburst scaffold.

(E and F) Quantification of ooDSGC (E) and starburst (F) laminar errors in *Flrt2*[Ret] mutants; *Unc5c*^{−/−} mutants; and wild-type littermate controls. P15 data are replotted from Figure 2 to facilitate comparisons with younger ages. Differences between mutant and controls do not arise until P15 (ooDSGCs) or P10 (starbursts). Statistics (E and F) Kruskal-Wallis test; p values on graph are for main effect of genotype at each age. Sample sizes: P6 control n = 7; P6 *Flrt2*[Ret] n = 8; P6 *Unc5c*^{−/−} n = 4; P10 control n = 8; P10 *Flrt2*[Ret] n = 4 (E) or n = 5 (F); P10 *Unc5c*^{−/−} n = 6.

Scale bars, 20 μm (scale bar in A also applies to B). Error bars, SEM.
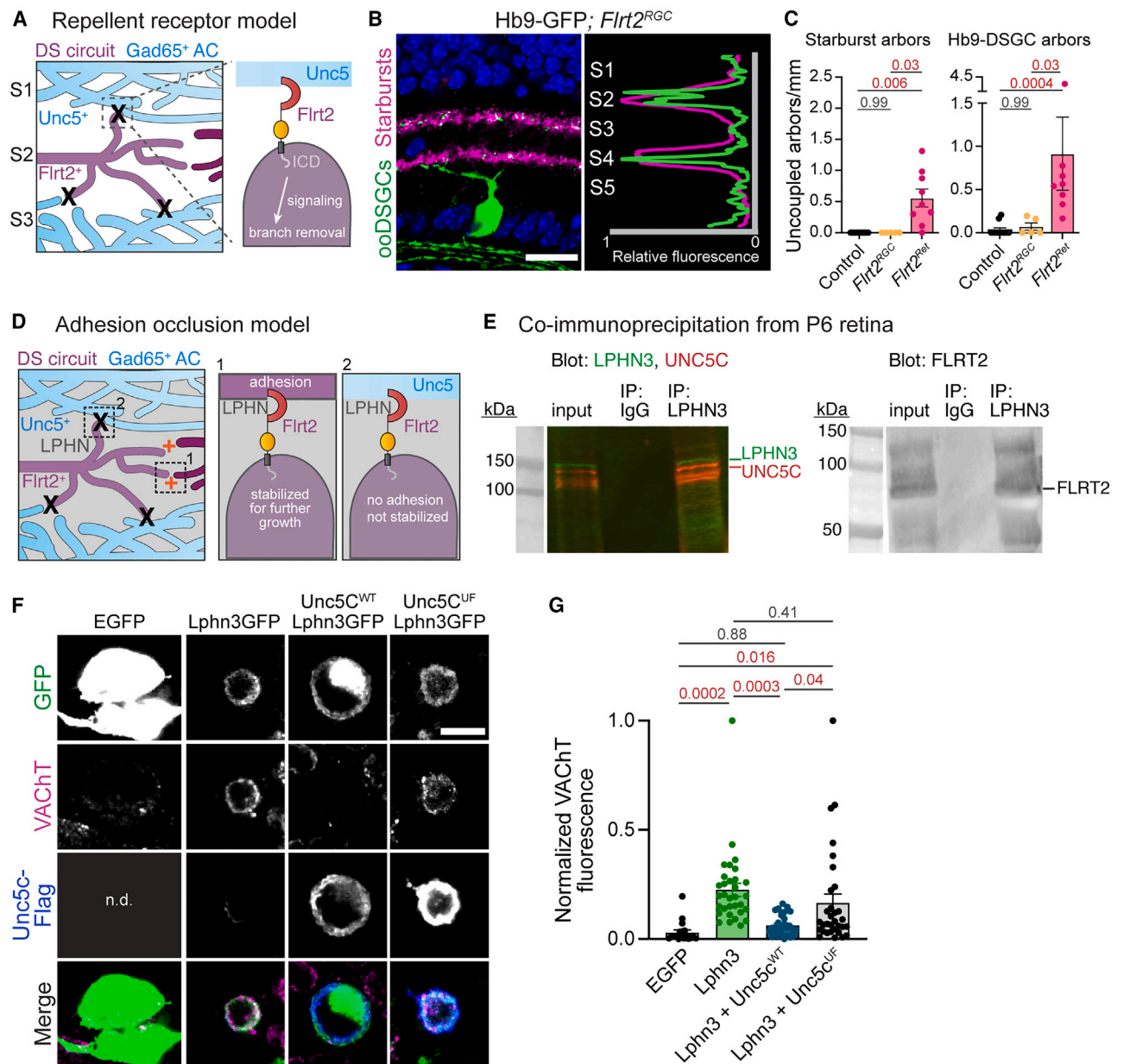
Also see Figure S6.

Figure 6. UNC5s function by occluding FLRT-LPHN adhesion

(A) Illustration of repellent receptor model: FLRT2 transduces repulsive signals upon UNC5 binding, driving elimination of mistargeted dendrite branches (X). Model predicts cell-autonomous requirement for FLRT2 within ooDSGCs. ICD, intracellular domain.

(B and C) Deletion of *Flrt2* from RGCs (*Flrt2^RGC* mutants) rules out repellent receptor model. (B) Representative image (left) and profile plots (right) showing normal dendrite targeting of Hb9-ooDSGCs (anti-GFP) and starbursts (anti-VAChT) in *Flrt2^RGC* mutants. (C) Quantification of mistargeted dendrites. Sample sizes: littermate controls, n = 9; *Flrt2^RGC* n = 5. For comparison, *Flrt2^Ret* data are replotted from Figure 2. Statistics, Kruskal-Wallace test with post hoc Dunn's test. p values (shown on graph) were corrected for multiple comparisons.

(D) Illustration of adhesion-occlusion model: LPHN protein (gray) localizes throughout IPL, including starburst and ooDSGC dendrites; UNC5s are in non-DS sublayers. Dendritic contacts among DS circuit neurons are stabilized (orange +) by transcellular reciprocal FLRT2-LPHN adhesion (inset 1). Contacts with inappropriate partners also result in FLRT2-LPHN binding, but these are not stabilized (X) due to the presence of UNC5 which occludes FLRT2-LPHN adhesion (inset 2).

(E) Co-immunoprecipitation indicates LPHN3-UNC5C-FLRT2 complex is present in P6 retina. UNC5C (left) and FLRT2 (right) are enriched in LPHN3 pull-down condition compared with input lysates or to IgG pull-down control. Upper FLRT2 band (just below 150 kDa) likely corresponds to FLRT2 dimer.

(F and G) Adhesion assay using primary retinal neurons co-cultured with HEK cells. (F) Representative images of VAChT⁺ starburst arbors associating with HEK cells transfected as indicated; (G) quantification of VAChT fluorescence surrounding HEK cells. Starburst arbors encircle HEK cells transfected with LPHN3-GFP, but not GFP alone. Starburst-LPHN3 adhesion is blocked by co-transfection of FLAG-tagged wild-type (WT) UNC5C, but not UNC5C^UF mutant that cannot bind
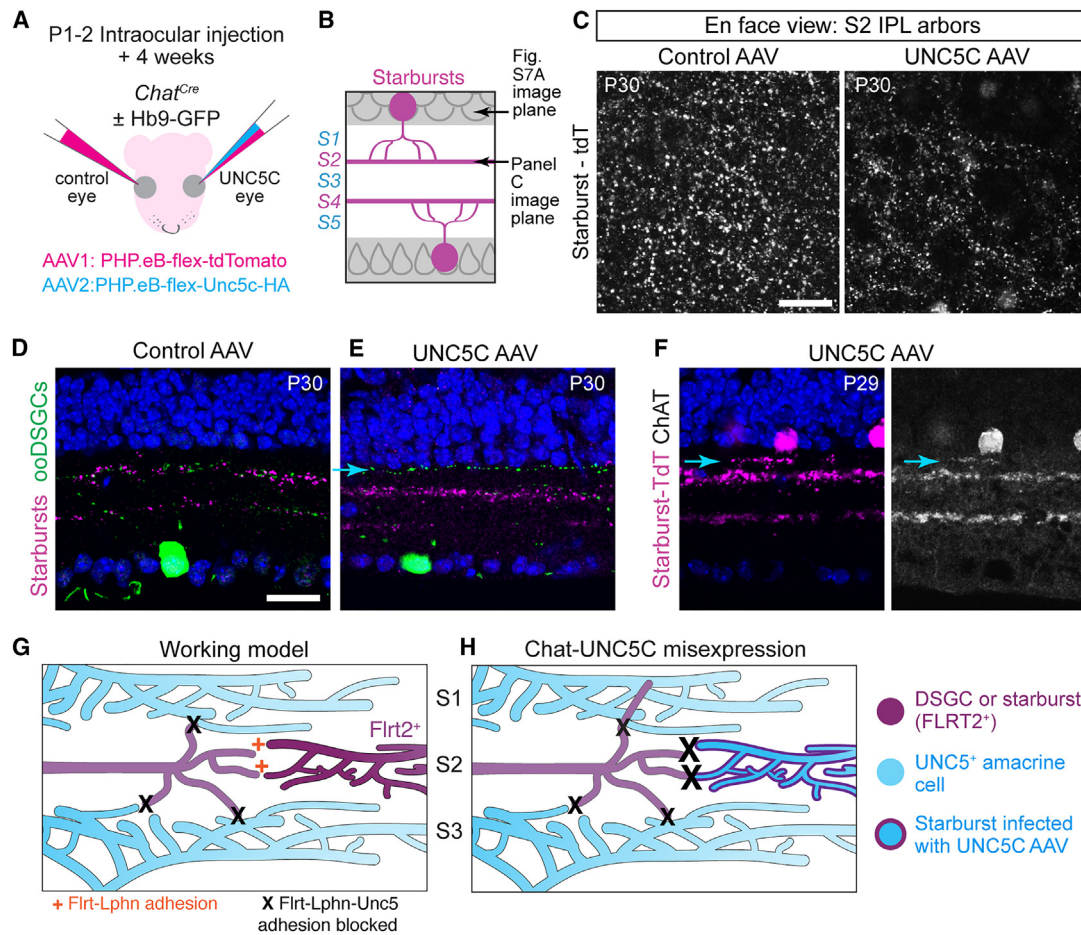
(legend continued on next page)

Figure 7. Misexpression of UNC5C in starburst cells induces DS circuit laminar targeting errors

(A) Strategy for starburst-specific flex-switch AAV expression in *Chat^Cre* mice. PHP.eB, AAV serotype.

(B) Illustration showing confocal imaging planes used for whole-mount analysis of AAV-infected retinas (C, Figure S7A).

(C) Starburst dendritic density is diminished by UNC5C misexpression. En-face views of tdTomato (tdT)⁺ OFF starburst dendrites in retinal whole mounts infected with specified AAVs (B shows imaging plane). Representative images of tdT-only control group (left; n = 4) and UNC5C misexpression group (right, n = 5). Lower dendrite density in UNC5C group is not explained by a difference in number of infected starburst cells (Figure S7A).

(D–F) Representative cross-sections showing IPL projections of starburst (magenta, anti-tdTomato; white, anti-ChAT) and Hb9-ooDSGC (green, anti-GFP) dendrites in retinas infected with specified AAVs. Laminar targeting is normal in retinas expressing tdTomato alone (D; n = 4 mice) but is disrupted by Chat-UNC5C misexpression (E, Hb9-DSGCs, n = 4 mice; F, starbursts, n = 5 mice).

(G and H) Working model for FLRT2-UNC5C function. During normal development (G), FLRT2⁺ DS circuit dendrites branch exuberantly as they grow. Properly stratified branches are stabilized by FLRT-LPHN adhesion (+). Branches that stray into adjacent IPL layers contact UNC5⁺ amacrine arbors; this blocks FLRT-LPHN adhesion leading to branch elimination (X). Upon Chat-UNC5C misexpression (H), correctly targeted arbors in S2 receive a large UNC5 signal (large X), thereby diminishing FLRT2-LPHN adhesion and suppressing growth. Ectopic UNC5 signal may be larger than endogenous UNC5 signal (small X). Survival and growth of mistargeted arbors indicates that neurons compare relative levels of UNC5 signaling—and hence relative levels of FLRT2-LPHN positive signals— across their dendritic branches to determine which branches will survive.

Scale bars: 20 μm. Scale bar in (D) applies to (E) and (F).

Also see Figure S7.

which the stable portion of an arbor sprouts numerous transient processes.[72,73] Only a small subset of these sprouts survive to become part of the mature arbor.[74–77] Given this growth mechanism, it is plausible that DS circuit dendrites cannot expand in the tangential plane without inadvertently sprouting out of their sub-

layers. In this case, the FLRT2-UNC5-LPHN system could serve to distinguish correctly targeted dendritic sprouts from mistargeted ones.

Under this model (Figure 7G), correctly targeted DS circuit dendritic sprouts experience stronger FLRT2-LPHN adhesion

FLRTs. n.d., staining was not performed. Statistics: one-way ANOVA with Tukey's post hoc test. p values were corrected for multiple comparisons. Sample sizes (number of cells): n = 18 EGFP; n = 32 Lphn3 alone; n = 31 Lphn3 + Unc5c^WT; n = 32 Lphn3 + Unc5c^UF. Data from three independent culture experiments. Scale bars: 20 μm in (B) and 10 μm in (F). Error bars (C and G), SEM.

Also see Figure S6.

than mistargeted sprouts contacting adjacent layers, where UNC5s interfere with FLRT-LPHN adhesion. Adhesion is a powerful pro-survival cue for nascent dendrite branches, not least because it promotes synaptogenesis[74,78] Thus, branches that experience more FLRT2-LPHN adhesion should be more likely to survive, to acquire synapses,[34,39] and to become part of the mature dendrite tree. This model is strongly supported by our *in vivo* experiments. In wild-type retina, the adhesion differential between correct and mistargeted branches may be so great that the chance of mistargeted sprouts surviving is close to zero. However, the genetic manipulations we performed here are expected to alter this adhesion differential—either by increasing adhesion of mistargeted arbors, as when UNC5s are removed or when FLRT2 is unable to bind UNC5s; or by diminishing adhesion of correctly targeted arbors, as when starburst cells lose FLRT2 or ectopically express UNC5C. In all of these cases, mistargeted branches should experience greater relative FLRT2-LPHN adhesion, leading to stochastic stabilization of a subset of these branches which ultimately mature to become ectopic DS circuit IPL arbors. Thus, each of our genetic experiments is consistent with the working model (Figures 7G and 7H).

Limitations of the study

Here, we focused on FLRT2, UNC5C, and UNC5D, but other molecules also have important roles in DS circuit formation. This is evident from the fact that manipulation of FLRT2-UNC5 signaling did not prevent circuit assembly, and persistent laminar errors were seen in only a subset of ooDSGCs and OFF starburst cells. ON starbursts, meanwhile, stratified independently of FLRT2 and UNC5s. Because FLRT2-UNC5 signaling impacts pruning and refinement, rather than initial pairing of synaptic partners, it would have been surprising to find that disrupting this system completely breaks the DS circuit. Instead, pruning failures are expected to append ectopic dendrites onto the normal arbor, as we indeed observed (Figures 2K–2M). Nevertheless, the relatively limited nature of these phenotypes suggests that future work is needed to identify other molecular families that also contribute to DS circuit refinement.

Even within the gene families studied here, multiple FLRTs, UNC5s, and LPHNs are present in developing retina and poised to compensate for the loss of a single gene.[79–81] There is precedent for redundancy in DS circuit assembly: to completely disrupt adhesion between starburst and ooDSGC dendrites during the P0–P6 period, it was necessary to simultaneously knock out three cadherin genes.[28] Therefore, a more thorough disruption of the FLRT-UNC5-LPHN system might produce more profound phenotypes. We attempted to generate *Unc5c; Unc5d* double mutants but unfortunately these animals died at birth. Further work will therefore be needed to understand the full phenotypic consequences of disrupting FLRT-UNC5-LPHN signals.

STAR★METHODS

Detailed methods are provided in the online version of this paper and include the following:

- **KEY RESOURCES TABLE**

- **RESOURCE AVAILABILITY**
  - Lead contact
  - Materials availability
  - Data and code availability
- **EXPERIMENTAL MODEL AND STUDY PARTICIPANT DETAILS**
  - Mice
  - Primary cultures and cell lines
- **METHOD DETAILS**
  - Generation of *Flrt2^{UF}* mice
  - Cell culture
  - In situ hybridization
  - Single cell RNA-seq
  - Immunohistochemistry
  - Western blots and co-immunoprecipitation
  - Synapse density in IPL
  - Synapse identification on ooDSGC dendrites
  - Analysis of laminar targeting phenotypes
  - Two-photon guided morphological reconstructions
  - UNC5C gain of function
- **QUANTIFICATION AND STATISTICAL ANALYSIS**

REFERENCES

1. Sanes, J.R., and Zipursky, S.L. (2020). Synaptic specificity, recognition molecules, and assembly of neural circuits. Cell *181*, 536–556. https://doi.org/10.1016/j.cell.2020.04.008.

2. Prigge, C.L., and Kay, J.N. (2018). Dendrite morphogenesis from birth to adulthood. Curr. Opin. Neurobiol. *53*, 139–145. https://doi.org/10.1016/j.conb.2018.07.007.

3. Lefebvre, J.L., Sanes, J.R., and Kay, J.N. (2015). Development of dendritic form and function. Annu. Rev. Cell Dev. Biol. *31*, 741–777. https://doi.org/10.1146/annurev-cellbio-100913-013020.

4. Pecho-Vrieseling, E., Sigrist, M., Yoshida, Y., Jessell, T.M., and Arber, S. (2009). Specificity of sensory–motor connections encoded by Sema3e–Plxnd1 recognition. Nature *459*, 842–846. https://doi.org/10.1038/nature08000.

5. Kolodkin, A.L., and Tessier-Lavigne, M. (2011). Mechanisms and molecules of neuronal wiring: a primer. Cold Spring Harb. Perspect. Biol. *3*, 1–14. https://doi.org/10.1101/cshperspect.a001727.

6. Cang, J., and Feldheim, D.A. (2013). Developmental mechanisms of topographic map formation and alignment. Annu. Rev. Neurosci. *36*, 51–77. https://doi.org/10.1146/annurev-neuro-062012-170341.

7. Pederick, D.T., Lui, J.H., Gingrich, E.C., Xu, C., Wagner, M.J., Liu, Y., He, Z., Quake, S.R., and Luo, L. (2021). Reciprocal repulsions instruct the precise assembly of parallel hippocampal networks. Science *372*, 1068–1073. https://doi.org/10.1126/science.abg1774.

8. Sun, L.O., Jiang, Z., Rivlin-Etzion, M., Hand, R., Brady, C.M., Matsuoka, R.L., Yau, K.W., Feller, M.B., and Kolodkin, A.L. (2013). On and off retinal circuit assembly by divergent molecular mechanisms. Science *342*, 1241974. https://doi.org/10.1126/science.1241974.

9. Matsuoka, R.L., Nguyen-Ba-Charvet, K.T., Parray, A., Badea, T.C., Chédotal, A., and Kolodkin, A.L. (2011). Transmembrane semaphorin signalling controls laminar stratification in the mammalian retina. Nature *470*, 259–263. https://doi.org/10.1038/nature09675.

10. Ray, T.A., Roy, S., Kozlowski, C., Wang, J., Cafaro, J., Hulbert, S.W., Wright, C.V.E., Field, G.D., and Kay, J.N. (2018). Formation of retinal direction-selective circuitry initiated by starburst amacrine cell homotypic contact. eLife *7*, e34241. https://doi.org/10.7554/eLife.34241.

11. Visser, J.J., Cheng, Y., Perry, S.C., Chastain, A.B., Parsa, B., Masri, S.S., Ray, T.A., Kay, J.N., and Wojtowicz, W.M. (2015). An extracellular biochemical screen reveals that FLRTs and Unc5s mediate neuronal subtype recognition in the retina. eLife *4*, e08149. https://doi.org/10.7554/eLife.08149.

12. Patterson, S.S., Bembry, B.N., Mazzaferri, M.A., Neitz, M., Rieke, F., Soetedjo, R., and Neitz, J. (2022). Conserved circuits for direction selectivity in the primate retina. Curr. Biol. *32*, 2529–2538.e4. https://doi.org/10.1016/j.cub.2022.04.056.

13. Kim, Y.J., Peterson, B.B., Crook, J.D., Joo, H.R., Wu, J., Puller, C., Robinson, F.R., Gamlin, P.D., Yau, K.W., Viana, F., et al. (2022). Origins of direction selectivity in the primate retina. Nat. Commun. *13*, 2862. https://doi.org/10.1038/s41467-022-30405-5.

14. Mauss, A.S., Vlasits, A., Borst, A., and Feller, M. (2017). Visual circuits for direction selectivity. Annu. Rev. Neurosci. *40*, 211–230. https://doi.org/10.1146/annurev-neuro-072116-031335.

15. Giolli, R.A., Blanks, R.H., and Lui, F. (2006). The accessory optic system: basic organization with an update on connectivity, neurochemistry, and function. Prog. Brain Res. *151*, 407–440. https://doi.org/10.1016/S0079-6123(05)51013-6.

16. Fredericks, C.A., Giolli, R.A., Blanks, R.H., and Sadun, A.A. (1988). The human accessory optic system. Brain Res. *454*, 116–122. https://doi.org/10.1016/0006-8993(88)90809-8.

17. Hamilton, N.R., Scasny, A.J., and Kolodkin, A.L. (2021). Development of the vertebrate retinal direction-selective circuit. Dev. Biol. *477*, 273–283. https://doi.org/10.1016/j.ydbio.2021.06.004.

18. Ray, T.A., and Kay, J.N. (2015). Following directions from the retina to the brain. Neuron *86*, 855–857. https://doi.org/10.1016/j.neuron.2015.05.017.

19. Briggman, K.L., Helmstaedter, M., and Denk, W. (2011). Wiring specificity in the direction-selectivity circuit of the retina. Nature *471*, 183–188. https://doi.org/10.1038/nature09818.

20. Fried, S.I., Münch, T.A., and Werblin, F.S. (2002). Mechanisms and circuitry underlying directional selectivity in the retina. Nature *420*, 411–414. https://doi.org/10.1038/nature01179.

21. Yoshida, K., Watanabe, D., Ishikane, H., Tachibana, M., Pastan, I., and Nakanishi, S. (2001). A key role of starburst amacrine cells in originating retinal directional selectivity and optokinetic eye movement. Neuron *30*, 771–780.

22. Hanson, L., Sethuramanujam, S., deRosenroll, G., Jain, V., and Awatramani, G.B. (2019). Retinal direction selectivity in the absence of asymmetric starburst amacrine cell responses. eLife *8*. https://doi.org/10.7554/eLife.42392.

23. Vaney, D.I., and Pow, D.V. (2000). The dendritic architecture of the cholinergic plexus in the rabbit retina: selective labeling by glycine accumulation in the presence of sarcosine. J. Comp. Neurol. *421*, 1–13.

24. Pei, Z., Chen, Q., Koren, D., Giammarinaro, B., Acaron Ledesma, H., and Wei, W. (2015). Conditional knock-out of vesicular GABA transporter gene from starburst amacrine cells reveals the contributions of multiple synaptic mechanisms underlying direction selectivity in the retina. J. Neurosci. *35*, 13219–13232. https://doi.org/10.1523/JNEUROSCI.0933-15.2015.

25. Bleckert, A., Zhang, C., Turner, M.H., Koren, D., Berson, D.M., Park, S.J.H., Demb, J.B., Rieke, F., Wei, W., and Wong, R.O. (2018). GABA release selectively regulates synapse development at distinct inputs on direction-selective retinal ganglion cells. Proc. Natl. Acad. Sci. USA *115*, E12083–E12090. https://doi.org/10.1073/pnas.1803490115.

26. Sivyer, B., Tomlinson, A., and Taylor, W.R. (2019). Simulated saccadic stimuli suppress ON-type direction-selective retinal ganglion cells via glycinergic inhibition. J. Neurosci. *39*, 4312–4322. https://doi.org/10.1523/JNEUROSCI.3066-18.2019.

27. Stacy, R.C., and Wong, R.O.L. (2003). Developmental relationship between cholinergic amacrine cell processes and ganglion cell dendrites of the mouse retina. J. Comp. Neurol. *456*, 154–166. https://doi.org/10.1002/cne.10509.

28. Duan, X., Krishnaswamy, A., Laboulaye, M.A., Liu, J., Peng, Y.R., Yamagata, M., Toma, K., and Sanes, J.R. (2018). Cadherin combinations recruit dendrites of distinct retinal neurons to a shared interneuronal scaffold. Neuron *99*, 1145–1154.e6. https://doi.org/10.1016/j.neuron.2018.08.019.

29. Peng, Y.R., Tran, N.M., Krishnaswamy, A., Kostadinov, D., Martersteck, E.M., and Sanes, J.R. (2017). Satb1 regulates Contactin 5 to pattern dendrites of a mammalian retinal ganglion cell. Neuron *95*, 869–883.e6. https://doi.org/10.1016/j.neuron.2017.07.019.

30. Duan, X., Krishnaswamy, A., De la Huerta, I., and Sanes, J.R. (2014). Type II cadherins guide assembly of a direction-selective retinal circuit. Cell *158*, 793–807. https://doi.org/10.1016/j.cell.2014.06.047.

31. Klein, R., and Pasterkamp, R.J. (2021). Recent advances in inter-cellular interactions during neural circuit assembly. Curr. Opin. Neurobiol. *69*, 25–32. https://doi.org/10.1016/j.conb.2020.12.004.

32. Jackson, V.A., Mehmood, S., Chavent, M., Roversi, P., Carrasquero, M., del Toro, D., Seyit-Bremer, G., Ranaivoson, F.M., Comoletti, D., Sansom, M.S.P., et al. (2016). Super-complexes of adhesion GPCRs and neural guidance receptors. Nat. Commun. *7*, 11184. https://doi.org/10.1038/ncomms11184.

33. Seiradake, E., del Toro, D., Nagel, D., Cop, F., Härtl, R., Ruff, T., Seyit-Bremer, G., Harlos, K., Border, E.C., Acker-Palmer, A., et al. (2014). FLRT structure: balancing repulsion and cell adhesion in cortical and vascular development. Neuron *84*, 370–385. https://doi.org/10.1016/j.neuron.2014.10.008.

34. O'Sullivan, M.L., de Wit, J., Savas, J.N., Comoletti, D., Otto-Hitt, S., Yates, J.R., and Ghosh, A. (2012). FLRT proteins are endogenous latrophilin

ligands and regulate excitatory synapse development. Neuron *73*, 903–910. https://doi.org/10.1016/j.neuron.2012.01.018.

35. Yamagishi, S., Hampel, F., Hata, K., Del Toro, D., Schwark, M., Kvachnina, E., Bastmeyer, M., Yamashita, T., Tarabykin, V., Klein, R., et al. (2011). FLRT2 and FLRT3 act as repulsive guidance cues for Unc5-positive neurons. EMBO J. *30*, 2920–2933. https://doi.org/10.1038/emboj.2011.189.

36. Ranaivoson, F.M., Liu, Q., Martini, F., Bergami, F., von Daake, S., Li, S., Lee, D., Demeler, B., Hendrickson, W.A., and Comoletti, D. (2015). Structural and mechanistic insights into the Latrophilin3-FLRT3 complex that mediates glutamatergic synapse development. Structure *23*, 1665–1677. https://doi.org/10.1016/j.str.2015.06.022.

37. Lu, Y.C., Nazarko, O.V., Sando, R., Salzman, G.S., Li, N.S., Südhof, T.C., and Araç, D. (2015). Structural basis of Latrophilin-FLRT-UNC5 interaction in cell adhesion. Structure *23*, 1678–1691. https://doi.org/10.1016/j.str.2015.06.024.

38. Jackson, V.A., del Toro, D., Carrasquero, M., Roversi, P., Harlos, K., Klein, R., and Seiradake, E. (2015). Structural basis of latrophilin-FLRT interaction. Structure *23*, 774–781. https://doi.org/10.1016/j.str.2015.01.013.

39. Sando, R., Jiang, X., and Südhof, T.C. (2019). Latrophilin GPCRs direct synapse specificity by coincident binding of FLRTs and teneurins. Science *363*, eaav7969. https://doi.org/10.1126/science.aav7969.

40. del Toro, D., Carrasquero-Ordaz, M.A., Chu, A., Ruff, T., Shahin, M., Jackson, V.A., Chavent, M., Berbeira-Santana, M., Seyit-Bremer, G., Brignani, S., et al. (2020). Structural basis of teneurin-latrophilin interaction in repulsive guidance of migrating neurons. Cell *180*, 323–339.e19. https://doi.org/10.1016/j.cell.2019.12.014.

41. Famiglietti, E.V., and Sundquist, S.J. (2010). Development of excitatory and inhibitory neurotransmitters in transitory cholinergic neurons, starburst amacrine cells, and GABAergic amacrine cells of rabbit retina, with implications for previsual and visual development of retinal ganglion cells. Vis. Neurosci. *27*, 19–42. https://doi.org/10.1017/S0952523810000052.

42. Yan, W., Laboulaye, M.A., Tran, N.M., Whitney, I.E., Benhar, I., and Sanes, J.R. (2020). Mouse retinal cell atlas: molecular identification of over sixty amacrine cell types. J. Neurosci. *40*, 5177–5195. https://doi.org/10.1523/JNEUROSCI.0471-20.2020.

43. Furuta, Y., Lagutin, O., Hogan, B.L., and Oliver, G.C. (2000). Retina- and ventral forebrain-specific Cre recombinase activity in transgenic mice. Genesis *26*, 130–132.

44. Trenholm, S., Johnson, K., Li, X., Smith, R.G., and Awatramani, G.B. (2011). Parallel mechanisms encode direction in the retina. Neuron *71*, 683–694. https://doi.org/10.1016/j.neuron.2011.06.020.

45. Huberman, A.D., Wei, W., Elstrott, J., Stafford, B.K., Feller, M.B., and Barres, B.A. (2009). Genetic identification of an On-Off direction-selective retinal ganglion cell subtype reveals a layer-specific subcortical map of posterior motion. Neuron *62*, 327–334. https://doi.org/10.1016/j.neuron.2009.04.014.

46. Kay, J.N., De la Huerta, I., Kim, I.J., Zhang, Y., Yamagata, M., Chu, M.W., Meister, M., and Sanes, J.R. (2011). Retinal ganglion cells with distinct directional preferences differ in molecular identity, structure, and central projections. J. Neurosci. *31*, 7753–7762. https://doi.org/10.1523/JNEUROSCI.0907-11.2011.

47. Kim, D., and Ackerman, S.L. (2011). The UNC5C Netrin receptor regulates dorsal guidance of mouse hindbrain axons. J. Neurosci. *31*, 2167–2179. https://doi.org/10.1523/JNEUROSCI.5254-10.2011.

48. Ackerman, S.L., Kozak, L.P., Przyborski, S.A., Rund, L.A., Boyer, B.B., and Knowles, B.B. (1997). The mouse rostral cerebellar malformation gene encodes an UNC-5-like protein. Nature *386*, 838–842. https://doi.org/10.1038/386838a0.

49. Fleitas, C., Marfull-Oromí, P., Chauhan, D., Del Toro, D., Peguera, B., Zammou, B., Rocandio, D., Klein, R., Espinet, C., and Egea, J. (2021). FLRT2 and FLRT3 cooperate in maintaining the tangential migratory streams of cortical interneurons during development. J. Neurosci. *41*, 7350–7362. https://doi.org/10.1523/JNEUROSCI.0380-20.2021.

50. Mani, A., Yang, X., Zhao, T., Leyrer, M.L., Schreck, D., and Berson, D.M. (2022). A retinal circuit that vetoes optokinetic responses to fast visual motion. Preprint at bioRxiv. https://doi.org/10.1101/2021.10.31.466688.

51. Della Santina, L., Inman, D.M., Lupien, C.B., Horner, P.J., and Wong, R.O.L. (2013). Differential progression of structural and functional alterations in distinct retinal ganglion cell types in a mouse model of glaucoma. J. Neurosci. *33*, 17444–17457. https://doi.org/10.1523/JNEUROSCI.5461-12.2013.

52. Tiriac, A., Bistrong, K., Pitcher, M.N., Tworig, J.M., and Feller, M.B. (2022). The influence of spontaneous and visual activity on the development of direction selectivity maps in mouse retina. Cell Rep. *38*, 110225. https://doi.org/10.1016/j.celrep.2021.110225.

53. Wei, W., Hamby, A.M., Zhou, K., and Feller, M.B. (2011). Development of asymmetric inhibition underlying direction selectivity in the retina. Nature *469*, 402–406. https://doi.org/10.1038/nature09600.

54. Yonehara, K., Balint, K., Noda, M., Nagel, G., Bamberg, E., and Roska, B. (2011). Spatially asymmetric reorganization of inhibition establishes a motion-sensitive circuit. Nature *469*, 407–410. https://doi.org/10.1038/nature09711.

55. Fisher, L.J. (1979). Development of synaptic arrays in the inner plexiform layer of neonatal mouse retina. J. Comp. Neurol. *187*, 359–372. https://doi.org/10.1002/cne.901870207.

56. Lefebvre, J.L., Kostadinov, D., Chen, W.V., Maniatis, T., and Sanes, J.R. (2012). Protocadherins mediate dendritic self-avoidance in the mammalian nervous system. Nature *488*, 517–521. https://doi.org/10.1038/nature11305.

57. Kim, I.J., Zhang, Y., Meister, M., and Sanes, J.R. (2010). Laminar restriction of retinal ganglion cell dendrites and axons: subtype-specific developmental patterns revealed with transgenic markers. J. Neurosci. *30*, 1452–1462. https://doi.org/10.1523/JNEUROSCI.4779-09.2010.

58. Leyva-Díaz, E., del Toro, D., Menal, M.J., Cambray, S., Susín, R., Tessier-Lavigne, M., Klein, R., Egea, J., and López-Bendito, G. (2014). FLRT3 is a Robo1-interacting protein that determines Netrin-1 attraction in developing axons. Curr. Biol. *24*, 494–508. https://doi.org/10.1016/j.cub.2014.01.042.

59. Kay, J.N., Chu, M.W., and Sanes, J.R. (2012). MEGF10 and MEGF11 mediate homotypic interactions required for mosaic spacing of retinal neurons. Nature *483*, 465–469. https://doi.org/10.1038/nature10877.

60. Rheaume, B.A., Jereen, A., Bolisetty, M., Sajid, M.S., Yang, Y., Renna, K., Sun, L., Robson, P., and Trakhtenberg, E.F. (2018). Single cell transcriptome profiling of retinal ganglion cells identifies cellular subtypes. Nat. Commun. *9*, 2759. https://doi.org/10.1038/s41467-018-05134-3.

61. Tran, N.M., Shekhar, K., Whitney, I.E., Jacobi, A., Benhar, I., Hong, G., Yan, W., Adiconis, X., Arnold, M.E., Lee, J.M., et al. (2019). Single-cell profiles of retinal ganglion cells differing in resilience to injury reveal neuroprotective genes. Neuron *104*, 1039–1055.e12. https://doi.org/10.1016/j.neuron.2019.11.006.

62. Scheiffele, P., Fan, J., Choih, J., Fetter, R., and Serafini, T. (2000). Neuroligin expressed in nonneuronal cells triggers presynaptic development in contacting axons. Cell *101*, 657–669. https://doi.org/10.1016/s0092-8674(00)80877-6.

63. Sanes, J.R., and Zipursky, S.L. (2010). Design principles of insect and vertebrate visual systems. Neuron *66*, 15–36. https://doi.org/10.1016/j.neuron.2010.01.018.

64. Xie, X., Tabuchi, M., Brown, M.P., Mitchell, S.P., Wu, M.N., and Kolodkin, A.L. (2017). The laminar organization of the Drosophila ellipsoid body is semaphorin-dependent and prevents the formation of ectopic synaptic connections. eLife *6*, e25328. https://doi.org/10.7554/eLife.25328.

65. Murcia-Belmonte, V., Coca, Y., Vegar, C., Negueruela, S., de Juan Romero, C., Valiño, A.J., Sala, S., DaSilva, R., Kania, A., Borrell, V., et al. (2019). A retino-retinal projection guided by Unc5c emerged in species with retinal waves. Curr. Biol. *29*, 1149–1160.e4. https://doi.org/10.1016/j.cub.2019.02.052.

66. Yamada, M., Fujita, Y., Hayano, Y., Hayakawa, H., Baba, K., Mochizuki, H., and Yamashita, T. (2019). Increased expression of fibronectin leucine-rich transmembrane protein 3 in the dorsal root ganglion induces neuropathic pain in rats. J. Neurosci. 39, 7615–7627. https://doi.org/10.1523/JNEUROSCI.0295-19.2019.

67. Del Toro, D., Ruff, T., Cederfjäll, E., Villalba, A., Seyit-Bremer, G., Borrell, V., and Klein, R. (2017). Regulation of cerebral cortex folding by controlling neuronal migration via FLRT adhesion molecules. Cell 169, 621–635.e16. https://doi.org/10.1016/j.cell.2017.04.012.

68. Ando, T., Tai-Nagara, I., Sugiura, Y., Kusumoto, D., Okabayashi, K., Kido, Y., Sato, K., Saya, H., Navankasattusas, S., Li, D.Y., et al. (2022). Tumor-specific interendothelial adhesion mediated by FLRT2 facilitates cancer aggressiveness. J. Clin. Invest. 132. https://doi.org/10.1172/JCI153626.

69. Khani, M., Gibbons, E., Bras, J., and Guerreiro, R. (2022). Challenge accepted: uncovering the role of rare genetic variants in Alzheimer's disease. Mol. Neurodegener. 17, 3. https://doi.org/10.1186/s13024-021-00505-9.

70. Schroeder, A., Vanderlinden, J., Vints, K., Ribeiro, L.F., Vennekens, K.M., Gounko, N.V., Wierda, K.D., and de Wit, J. (2018). A modular organization of LRR protein-mediated synaptic adhesion defines synapse identity. Neuron 99, 329–344.e7. https://doi.org/10.1016/j.neuron.2018.06.026.

71. El-Quessny, M., Maanum, K., and Feller, M.B. (2020). Visual experience influences dendritic orientation but is not required for asymmetric wiring of the retinal direction selective circuit. Cell Rep. 31, 107844. https://doi.org/10.1016/j.celrep.2020.107844.

72. Wong, R.O.L., and Ghosh, A. (2002). Activity-dependent regulation of dendritic growth and patterning. Nat. Rev. Neurosci. 3, 803–812. https://doi.org/10.1038/nrn941.

73. Ing-Esteves, S., and Lefebvre, J.L. (2021). Time-lapse imaging of neuronal arborization using sparse adeno-associated virus labeling of genetically targeted retinal cell populations. J. Vis. Exp. https://doi.org/10.3791/62308.

74. Cline, H., and Haas, K. (2008). The regulation of dendritic arbor development and plasticity by glutamatergic synaptic input: a review of the synaptotrophic hypothesis. J. Physiol. 586, 1509–1517. https://doi.org/10.1113/jphysiol.2007.150029.

75. Niell, C.M., Meyer, M.P., and Smith, S.J. (2004). In vivo imaging of synapse formation on a growing dendritic arbor. Nat. Neurosci. 7, 254–260. https://doi.org/10.1038/nn1191.

76. Takeo, Y.H., Shuster, S.A., Jiang, L., Hu, M.C., Luginbuhl, D.J., Rülicke, T., Contreras, X., Hippenmeyer, S., Wagner, M.J., Ganguli, S., et al. (2021). GluD2- and Cbln1-mediated competitive interactions shape the dendritic arbors of cerebellar Purkinje cells. Neuron 109, 629–644.e8. https://doi.org/10.1016/j.neuron.2020.11.028.

77. Lohmann, C., Myhr, K.L., and Wong, R.O.L. (2002). Transmitter-evoked local calcium release stabilizes developing dendrites. Nature 418, 177–181. https://doi.org/10.1038/nature00850.

78. Südhof, T.C. (2018). Towards an understanding of synapse formation. Neuron 100, 276–293. https://doi.org/10.1016/j.neuron.2018.09.040.

79. Ruff, T., Peters, C., Matsumoto, A., Ihle, S.J., Morales, P.A., Gaitanos, L., Yonehara, K., Del Toro, D., and Klein, R. (2021). FLRT3 marks direction-selective retinal ganglion cells that project to the medial terminal nucleus. Front. Mol. Neurosci. 14, 790466. https://doi.org/10.3389/fnmol.2021.790466.

80. Shekhar, K., Whitney, I.E., Butrus, S., Peng, Y.R., and Sanes, J.R. (2022). Diversification of multipotential postmitotic mouse retinal ganglion cell precursors into discrete types. eLife 11. https://doi.org/10.7554/eLife.73809.

81. Goetz, J., Jessen, Z.F., Jacobi, A., Mani, A., Cooler, S., Greer, D., Kadri, S., Segal, J., Shekhar, K., Sanes, J.R., et al. (2022). Unified classification of mouse retinal ganglion cells using function, morphology, and gene expression. Cell Rep. 40, 111040. https://doi.org/10.1016/j.celrep.2022.111040.

82. Wang, Y., Cao, Y., Hays, C.L., Laboute, T., Ray, T.A., Guerrero-Given, D., Ahuja, A.S., Patil, D., Rivero, O., Kamasawa, N., et al. (2021). Adhesion GPCR latrophilin 3 regulates synaptic function of cone photoreceptors in a trans-synaptic manner. Proc. Natl. Acad. Sci. USA 118. https://doi.org/10.1073/pnas.2106694118.

83. Schindelin, J., Arganda-Carreras, I., Frise, E., Kaynig, V., Longair, M., Pietzsch, T., Preibisch, S., Rueden, C., Saalfeld, S., Schmid, B., et al. (2012). Fiji: an open-source platform for biological-image analysis. Nat. Methods 9, 676–682. https://doi.org/10.1038/nmeth.2019.

84. Stuart, T., Butler, A., Hoffman, P., Hafemeister, C., Papalexi, E., Mauck, W.M., Hao, Y., Stoeckius, M., Smibert, P., and Satija, R. (2019). Comprehensive integration of single-cell data. Cell 177, 1888–1902.e21. https://doi.org/10.1016/j.cell.2019.05.031.

85. Ippolito, D.M., and Eroglu, C. (2010). Quantifying synapses: an immunocytochemistry-based assay to quantify synapse number. J. Vis. Exp. 2270. https://doi.org/10.3791/2270.

86. Savage, J.T., Ramirez, J., Risher, W.C., Irala, D., and Eroglu, C. (2023). SynBot: an open-source image analysis software for automated quantification of synapses. Preprint at bioRxiv. https://doi.org/10.1101/2023.06.26.546578.

87. Modzelewski, A.J., Chen, S., Willis, B.J., Lloyd, K.C.K., Wood, J.A., and He, L. (2018). Efficient mouse genome engineering by CRISPR-EZ technology. Nat. Protoc. 13, 1253–1274. https://doi.org/10.1038/nprot.2018.012.

88. Peng, B.Y., Wang, Q., Luo, Y.H., He, J.F., Tan, T., and Zhu, H. (2018). A novel and quick PCR-based method to genotype mice with a leptin receptor mutation (db/db mice). Acta Pharmacol. Sin. 39, 117–123. https://doi.org/10.1038/aps.2017.52.

89. Jiang, W., Gong, J., Rong, Y., and Yang, X. (2019). A new co-culture method for identifying synaptic adhesion molecules involved in synapse formation. Biophys. Rep. 5, 91–97. https://doi.org/10.1007/s41048-019-0084-4.

90. Manders, E.M., Stap, J., Brakenhoff, G.J., van Driel, R., and Aten, J.A. (1992). Dynamics of three-dimensional replication patterns during the S-phase, analysed by double labelling of DNA and confocal microscopy. J. Cell Sci. 103, 857–862. https://doi.org/10.1242/jcs.103.3.857.

91. Koh, S., Chen, W.J., Dejneka, N.S., Harris, I.R., Lu, B., Girman, S., Saylor, J., Wang, S., and Eroglu, C. (2018). Subretinal human umbilical tissue-derived cell transplantation preserves retinal synaptic connectivity and attenuates Müller glial reactivity. J. Neurosci. 38, 2923–2943. https://doi.org/10.1523/JNEUROSCI.1532-17.2018.

92. Longair, M.H., Baker, D.A., and Armstrong, J.D. (2011). Simple Neurite Tracer: open source software for reconstruction, visualization and analysis of neuronal processes. Bioinformatics 27, 2453–2454. https://doi.org/10.1093/bioinformatics/btr390.

93. El-Quessny, M., and Feller, M.B. (2021). Dendrite morphology minimally influences the synaptic distribution of excitation and inhibition in retinal direction-selective ganglion cells. eNeuro 8. https://doi.org/10.1523/ENEURO.0261-21.2021.

94. Schnütgen, F., Doerflinger, N., Calléja, C., Wendling, O., Chambon, P., and Ghyselinck, N.B. (2003). A directional strategy for monitoring Cre-mediated recombination at the cellular level in the mouse. Nat. Biotechnol. 21, 562–565. https://doi.org/10.1038/nbt811.

STAR★METHODS

KEY RESOURCES TABLE

REAGENT or RESOURCE	SOURCE	IDENTIFIER
Antibodies		
guinea pig anti-bassoon	Synaptic Systems	RRID: AB_2290619; Cat# 141004
goat anti-ChAT	Millipore	RRID: AB_2079751; Cat# AB144P
rabbit anti-FLRT2 (Western blot)	Thermo	Cat# PA5-109729
goat anti-FLRT2 (immunostaining)	R&D Systems	RRID: AB_2106600; Cat# AF2877
mouse anti-GAD65 clone GAD6	EMD Millipore	RRID: AB_2263126; Cat# MAB351
mouse anti-gephyrin clone mAb7a	Synaptic Systems	RRID: AB_2232546; Cat# 147021
rabbit anti-GFP	Millipore	RRID: AB_2630379; Cat# AB3080P
goat anti-GFP	Abcam	RRID: AB_304897; Cat# ab5450
rat anti-Neurofilament-M clone 2H3	Developmental Studies Hybridoma Bank	RRID: AB_531793; Cat# 2H3
rabbit anti-Satb1/2 clone EPR3951	Epitomics/Abcam	RRID:AB_10862207; Cat# ab109122
guinea pig anti-VAChT	Millipore	RRID: AB_2187981; Cat# AB1588
mouse anti-Flag clone M2	Sigma	RRID: AB_262044; Cat# F1804
mouse anti-LPHN3	Santa Cruz (see Wang et al.[82])	Cat# sc-393576
rabbit anti-UNC5C	NSJ	Cat# R31843
rat anti-hemagglutinin (HA)	Sigma	RRID: AB_390915; Cat# 11867423001
rabbit anti-mCherry (detects tdTomato)	Kerafast	Cat# EMU106
donkey anti-rabbit Alexa-488	Jackson Immunoresearch	RRID: AB_2313584; Cat# 711-545-152
donkey anti-goat Cy3	Jackson Immunoresearch	RRID: AB_2307351; Cat# 705-165-147
donkey anti-guinea pig Cy3	Jackson Immunoresearch	RRID: AB_2340460; Cat# 706-165-148
donkey anti-goat Alexa-647	Jackson Immunoresearch	RRID: AB_2340437; Cat# 705-605-147
donkey anti-guinea pig Alexa-647	Jackson Immunoresearch	RRID: AB_2340476; Cat# 706-605-148
donkey anti-mouse Alexa-647	Jackson Immunoresearch	RRID: AB_2340863; Cat# 715-605-151
donkey anti-rat Alexa-647	Jackson Immunoresearch	RRID: AB_2340694; Cat# 712-605-153
Bacterial and virus strains		
AAV: PHP.eB-CAG-flex-tdTomato-WPRE-pA	Gift of Edward Boyden (MIT) via Addgene	Addgene 28306-PHPeB
AAV: PHP.eB-CMV-flex-Unc5cHA-WPRE-SV40pA	Duke Viral Vector Core; this study	N/A
Chemicals, peptides, and recombinant proteins		
Protein A/G beads for immunoprecipitation	Pierce	Cat# 88803
Critical commercial assays		
HCR probeset: *Gad2*	Molecular Instruments	Probe lot# RTA798
HCR probeset: *Unc5c*	Molecular Instruments	Probe lot# RTB893
RNAScope probeset: *Gad2*	ACD	Cat# 439371
RNAScope probeset: *Unc5c*	ACD	Cat# 403211
Deposited data		
Amacrine cell scRNA-seq	Yan et al.[42]	Broad Single Cell Portal: SCP919
Adult RGC scRNA-seq	Tran et al.[61]	Broad Single Cell Portal: SCP509
Developing RGC scRNA-seq	Shekhar et al.[80]	Broad Single Cell Portal: SCP1706
Purified retinal neuron subtypes Affymetrix microarray	Kay et al.[59]	NCBI GEO: GSE35077
Experimental models: Cell lines		
HEK 293	ATCC	RRID: CVCL_0045; Cat#CRL-1573
Experimental models: Organisms/strains		
mouse: $Unc5c^{rcmTg(Ucp)1.23Kz}$ (*Unc5c* null)	Gift of Susan Ackerman (UCSD), see Ackerman et al.[48]	MGI:1857852

(Continued on next page)

Continued

REAGENT or RESOURCE	SOURCE	IDENTIFIER
mouse: *Unc5d*^{tm1Kln} (*Unc5d* null)	Gift of Viktor Tarabykin (Charité, Berlin), see Yamagishi et al.[35]	MGI:5495472
mouse: *Flrt2*^{tm1c(EUCOMM)Wtsi}/*RobH* (*Flrt2*^{flox})	EMMA repository	MGI:6119416
mouse: *Tg(Six3-cre)69Frty*	Jackson labs	RRID: IMSR_JAX: 019755
mouse: *Tg(Drd4-EGFP)W18Gsat*	Gift of Joshua Sanes (Harvard)	RRID: MMRRC_000231-UNC
mouse: *B6.Cg-Tg (Hlxb9-GFP)1Tmj/J* (Hb9-GFP)	Jackson labs	RRID: IMSR_JAX:005029
mouse: *Chat*^{tm2(cre)Lowl}	Jackson labs	RRID: IMSR_JAX:006410
mouse: *Slc17a6*^{tm2(cre)Lowl}/J (Vglut2^{Cre})	Jackson labs	RRID: IMSR_JAX:016963
mouse: *Flrt2*^{UF}	This study	RRID: IMSR_JAX:038570
mouse: CD-1	Charles River	RRID: IMSR_CRL:022
mouse: C57Bl6/J	Jackson labs	RRID: IMSR_JAX:000664
mouse: SJL/J	Jackson labs	RRID: IMSR_JAX:000686
mouse: B6SJLF1/J	Jackson labs	RRID: IMSR_JAX:100012
Oligonucleotides		
Flrt2^{UF} genotyping-outer F	IDT	TGGATGAGTTCCCCATGAACCTTC
Flrt2^{UF} genotyping-outer R	IDT	GAGATGATCGAAGACTCCTTGA GTTAACATTCGT
Flrt2^{UF} genotyping-inner F	IDT	GCGATTAGCCTCAAACTGTTGT TTTTATCGAAGAATAAT
Flrt2^{UF} genotyping-inner R	IDT	CAACAGGCACGCTACTCAGGTG
Flrt2^{UF} founder screening 1st PCR F	IDT	accgcggtggcggcc GCT CCT CAA GCT GGA AGA ACT CCA
Flrt2^{UF} founder screening 1st PCR R	IDT	tagaggatccactag TGT CTG ATA TGA CGG CAA TTC GGT
Flrt2^{UF} founder screening cloned fragment PCR F	IDT	caaggcgattaagttgggtaac
Flrt2^{UF} founder screening cloned fragment PCR R	IDT	gcgtgttcgaattcgccaatgac
sgRNA for generating *Flrt2*^{UF} genomic mutation (DNA template sequence)	This study	GCCCAACAGGCACGCTACTCagg
Repair oligo for generating *Flrt2*^{UF} genomic mutation	IDT	gctcctcaagctggaagaactccacctggac gacaactccatatctacagtgggagtagaag acggagcgttccgggaagcgattagcctca aactgttgtttttatcgaagaataatctgagtag cgtgcctgttgggcttcctgtagacttgcaag agctgagagtggatgaaaaccgaattgccg tcatatcagaca
Recombinant DNA		
plasmid: pAAV-CMV-flex-Unc5cHA-WPRE-SV40pA	This study	Addgene 205442
plasmid: pCMV-Lphn3-GFP	Gift of Matthew O'Sullivan (Duke), see O'Sullivan et al.[34]	N/A
plasmid: pTT3-Unc5c^{WT}-flag	Gift of Woj Wojtowicz (Stanford), see Visser et al.[11]	Addgene 72196
plasmid: pTT3-Unc5c^{UF}-flag	This study	N/A
Software and algorithms		
R version 4.1.2	https://cran.r-project.org/	RRID: SCR_001905
FIJI	Schindelin et al.[83]	RRID: SCR_002285
Seurat version 4.0	Stuart et al.[84]	RRID: SCR_007322
P5 RGC scRNAseq online viewer	Rheaume et al.[60]	https://health.uconn.edu/ neuroregeneration-lab/rgc-subtypes-gene-browser/

(Continued on next page)

Continued

REAGENT or RESOURCE	SOURCE	IDENTIFIER
Puncta Analyzer	Ippolito and Eroglu[85]; Savage et al.[86]	dx.doi.org/10.17504/protocols. io.3byl4qewjvo5/v1
Object Finder	Della Santina et al.[51]	https://zenodo.org/record/4767847

RESOURCE AVAILABILITY

Lead contact

Requests for resources and reagents should be directed to and will be fulfilled by the lead contact, Jeremy Kay (jeremy.kay@duke.edu)

Materials availability

The pAAV-CMV-flex-Unc5cHA-WPRE-SV40pA plasmid has been deposited at Addgene (ID #205442). Other plasmids used in this study may be obtained as noted in the key resources table or from the lead contact.

The $Flrt2^{UF}$ mouse line generated in this study has been deposited with the Jackson Laboratories repository (stock number 038570).

Data and code availability

- Existing, publicly available sequencing data were obtained from GEO or the Broad Institute Single Cell Portal (see key resources table). All microscopy and Western blot images are available upon request.
- ObjectFinder software is deposited at Zenodo. Puncta Analyzer software[85] (gift of C. Eroglu, Duke University) is available from the Eroglu lab. Please note that Puncta Analyzer has been deprecated and its key features are now incorporated into the newer SynBot software.[86] See key resources table for DOIs.
- Any additional information required to reanalyze the data reported in this paper is available from the lead contact upon request

EXPERIMENTAL MODEL AND STUDY PARTICIPANT DETAILS

Mice

Mouse experiments were performed according to protocols approved by the Institutional Animal Care and Use Committees at Duke University and University of California, Berkeley. Mice of both sexes were used for experiments, and we did not include or exclude animals on the basis of sex. CD1 mice were obtained from Charles River laboratory. $Flrt2^{flox}$ mice ($Flrt2^{tm1c(EUCOMM)Wtsi}/RobH$) were obtained from the EMMA repository (EM: 08315). Mice carrying the $Unc5c^{rcmTg(Ucp)1.23Kz}$ null allele[48] were a gift of Dr. Susan Ackerman (UCSD). $Unc5d^{tm1Kln}$ null mice[35] were a gift of Dr. Victor Tarabykin (Charité, Berlin) via Dr. David Feldheim (UCSC). Drd4-GFP ($Tg(Drd4-EGFP)W18Gsat$)) mice were a gift of Dr. Joshua Sanes. $Flrt2^{UF}$ mice were generated in this study as described in detail below. The following strains were obtained from Jackson Labs – see key resources table for catalog numbers: Hb9-GFP ($B6.Cg-Tg(Hlxb9-GFP)1Tmj/J$); Six3-Cre ($Tg(Six3-cre)69Frty)$); $Chat^{Cre}$ ($Chat^{tm2(cre)Lowl}/J$); $Vglut2^{Cre}$ ($Slc17a6^{tm2(cre)Lowl}/J$).

Mutant and transgenic strains were maintained on the C57Bl6/J background, and in most cases experimental animals were also on this background. For $Unc5c$ null mice, experimental animals were generated on a mixed C57-SJL background as follows: First, to generate breeders, heterozygous mutants ($Unc5c^{+/-}$) on the C57Bl6/J background were outcrossed to SJL/J. $Unc5c^{+/-}$ progeny from this cross were then bred to $Unc5c^{+/-}$ or Hb9-GFP; $Unc5c^{+/-}$ animals on the pure C57Bl6 background, thereby generating mutants and wild-type littermate controls for experiments. A similar breeding strategy was used for the $Flrt2^{UF}$ strain.

To generate $Flrt2^{Ret}$ mutants, $Six3-Cre; Flrt2^{flox/+}$ mice were bred to $Flrt2^{flox/+}$ or $Flrt2^{flox/flox}$ animals with or without the Hb9-GFP transgenes. These crosses yielded $Flrt2^{Ret}$ mutant animals of genotype $Six3-Cre; Flrt2^{flox/flox}$, as well as two types of wild-type controls 1) $Six3-Cre; Flrt2^{+/+}$ and 2) $flox/+$ or $flox/flox$ animals without the Cre transgene. These were phenotypically indistinguishable and so were pooled as $Flrt2^{WT}$ animals. A similar breeding strategy was used with $Vglut2^{Cre}$ mice to generate $Flrt2^{RGC}$ mutants.

For all strains, P1-P6 neonates were euthanized by ice anesthesia followed by decapitation. Mice aged P7 and older were euthanized via isoflurane anesthesia followed by decapitation.

Primary cultures and cell lines

Primary cultures of retinal neurons were prepared using P0/P1 mice obtained from CD1 timed pregnant litters (Charles River). Cultures were grown at 37° C in neuronal growth medium[89] containing MEM + B27 supplement and 5% fetal bovine serum.

HEK 293T cells were obtained from ATCC and grown at 37°C in DMEM containing 10% fetal bovine serum. For co-cultures with primary neurons, neuronal growth medium was used.

METHOD DETAILS

Generation of *Flrt2^UF* mice

To engineer the *Flrt2^UF* mutation (H170N)[33] into the mouse genome, we used a CRISPR-Cas9 homology-directed repair strategy. We generated a 200 bp repair oligonucleotide homologous to the region surrounding the codon encoding amino acid H170. In this oligonucleotide the CAC H170 codon was mutated to AAC (N). To induce homology-directed repair at the appropriate genomic site, a single guide RNA (sgRNA) was produced in which the PAM sequence overlaps the H170 codon (sequence 5' GCCCAA CAGGCACGCTACTCagg; PAM site is denoted by lowercase letters). The PAM sequence is destroyed by the codon-altering mutation, thereby rendering correctly edited alleles immune to further Cas9 cutting activity. See key resources table for sequences.

The repair DNA was electroporated into one-cell stage B6SJLF1/J embryos together with pre-assembled Cas9-sgRNA ribonucleoproteins, as described.[87] Briefly, to generate sgRNA for electroporation, a DNA template was generated by PCR and then used for RNA synthesis (HiScribe T7 RNA polymerase, NEB #E2040S). DNA template was removed from the reaction with Turbo DNAse (Invitrogen #AM2238). The sgRNA was purified by phenol/chloroform extraction, ethanol precipitated, and resuspended in nuclease-free H_2O. The Cas9 ribonucleoprotein was assembled by incubating Cas9 protein, sgRNA, and repair oligo together for 10 min at 37°C in Tris (2-carboxyethyl) phosphine hydrochloride (TCEP) buffer.[87] The ribonucleoprotein mix was electroporated using a NEPAGENE Super Electroporator (NEPA21 Type II) using a glass slide chamber with platinum electrodes (Bulldog Bio part CUY501P1-1.5) with the following settings: Poring Pulse: V 40, Length(ms) 3.5, Interval (ms)50, No 4, D. Rate % 10, Polarity +; Transfer Pulse: V 7, length (ms) 50, Interval (ms) 50, No. 5, D. Rate% 40, Polarity +/-. Following electroporation the embryos were transferred to pseudopregnant females.

To screen founders for the correctly modified allele, founder genomic DNA was prepared from tail and/or toe tissue and subject to PCR using primers targeting the ends of the repair oligonucleotide homology region (Sense: ' 5' accgcggtggcggcc GCT CCT CAA GCT GGA AGA ACT CCA 3'; Antisense: 5' tagaggatccactag TGT CTG ATA TGA CGG CAA TTC GGT 3'). PCR products were subject to Sanger sequencing using Sense primer. For animals in which sequencing revealed InDels across the target region, the PCR fragments containing InDels were cloned into pL253 at the NotI and SpeI sites via InFusion cloning (Takara #ST0344). Bacterial recombinants were screened via PCR using primers 253.S (caaggcgattaagttgggtaac) and 253.AS (gcgtgttcgaattcgccaatgac). Plasmid DNA from positive clones were sequenced using Sense primer for verification of the targeted mutation. Positive founders were backcrossed to C57Bl6/J. Subsequently, the line was maintained in the same manner.

To genotype the UF dinucleotide point mutation by PCR, we used a 4 primer strategy[88] in which "outer" primers in constant regions combine with "inner" primers overlapping the point mutation site to distinguish the wild-type and mutant alleles. Primer sequences are given in the key resources table. Band sizes: Outer, 599 bp. Inner mutant, 426 bp. Inner wild-type, 231 bp.

Cell culture

Primary cultures of P0/P1 retinal neurons were prepared from CD1 timed pregnant litters (Charles River). The procedure was modified from the protocol of Jiang et al.[89]. Retinas were isolated from the eyecup in dissecting solution,[89] followed by incubation in 0.5% Trypsin for 15-20 min at 37°C with gentle intermittent mixing. Next, trypsin was exchanged two times with dissecting solution and reaction was stopped using stopping solution (HBSS + 5% serum). Trypsinized retina was triturated 4 times either in stopping solution or MEM1X solution and centrifuged for 5 mins at 800 x g at 4°C. Cells were resuspended in 1.0 ml of plating medium[89] and filtered through 30 μm sterile filter. Isolated cells were plated at density of ≥ 200,000 cells/well on previously coated Poly L-lysine coverslips. Cells were allowed to settle for 30 mins in cell culture incubator, at which time 2 ml of plating medium was added into each well. Cells were incubated for 1 day at 37°C. On the next day, media was exchanged for neuronal growth medium[89] containing B27 supplement. On day 4, AraC (cytosine arabinoside) was included in the neuronal growth medium. Cultures were fixed on day 10-12.

For GAD65-VAChT, overlap analysis, confocal stacks were acquired from GAD65 + VAChT immunostained cultures and single z slices chosen for analysis. Overlap analysis[90] was performed with coloc2 ImageJ plugin. The overlap ratio was calculated as the VAChT pixel intensities within pixels containing non-zero GAD65 values, divided by total VAChT pixel intensity across the image. This yields a measure of overlap between the two signals that is independent of overall image brightness.[90]

For the co-culture cell adhesion assay, primary cultures were prepared as described above, and transfected HEK 293 cells were added to the culture on day 8. The day prior to co-culture, HEK cells were transfected with the following plasmids: CMV-EGFP; CMV-Lphn3-GFP encoding full-length LPHN3[34]; CMV-Unc5c-Flag encoding full-length UNC5C[11]; or CMV-Unc5c^UF-Flag encoding the mutant UNC5C protein that is impaired in binding FLRTs.[33] Transfected cells were co-cultured with primary cells for 2 days, then fixed in 2% paraformaldehyde/1x PBS and subjected to immunohistochemistry. Data are from three independent replicates of the experiment; these did not show significant batch effects so they were pooled for presentation in Figure 6G.

In situ hybridization

Eyes from euthanized P6 wildtype mice (CD-1 or B6;SJL strains) were fixed in 4% paraformaldehyde in PBS for 24 h at RT and then washed 3X with PBS. In situ hybridization was performed with two independent RNA labeling technologies – RNAScope (Advanced Cell Diagnostics, Newark, CA) and hybridization chain reaction (HCR; Molecular Instruments, Los Angeles, CA).

For RNAScope, isolated retinas were cryoprotected in 30% sucrose and 0.02% sodium azide in PBS and frozen in Tissue Freezing Medium (General Data; Cincinnati, OH). Retinas were cryosectioned at 16 μm and mounted on Superfrost Plus slides. Retinal sections were pre-treated according to manufacturer's instructions for fixed frozen tissue. Probes to *Unc5c* and *Gad2* (i.e. Gad65) were

from the standard ACD catalog. Probes were hybridized and amplified according to manufacturer's instructions using the RNAscope Fluorescent Multiplex Kit.

For HCR labeling, fixed eyes were methanol-habituated as follows: 5 min washes, rocking, on ice, first in 25% methanol, then 50% methanol, 75% methanol, and two 100% methanol washes. Eyecups were cryoprotected as above and cryosectioned at 20 μm. Sections were stained with in situ Hybridization Chain Reaction (HCR) probes for *Gad2* and *Unc5c*, from Molecular Instruments following Molecular Instruments' protocol for HCR RNA-FISH in fixed frozen tissue sections. The only deviations from this protocol are as follows: slides were treated with Proteinase K for 5 min; 0.8 μL of each probe was added to 150 μL probe hybridization buffer for each slide; slides were stained with Hoechst for 30 min at room temperature before amplification hairpins were washed off.

Following staining with either method, sections were imaged on a Nikon A1 confocal system. Z-stacks of 0.33 μm steps were acquired using a 60X objective (Plan Apochromat, NA 1.40) with oil immersion. Stacks were imported into FIJI[83]; single optical slices (or a Z-projection of a subset of the stack) are shown here for illustration purposes but the full Z-stack was used for quantification. To quantify RNA signals, the multi-point tool in FIJI was used to manually mark each nucleus that was positive for the probe. Positive cells were called based on the presence of punctate RNA signal overlapping the nuclear counterstain signal (Figure 1G). *Unc5c* and *Gad2* channels were analyzed individually to blind the co-expression analysis. Co-expression of markers was used to calculate fraction of *Unc5c* mRNA+ cells that expressed *Gad2* mRNA. Two sections were quantified for each animal.

Single cell RNA-seq
Single-cell RNA-seq data from FACS-purified amacrine cells,[42] adult RGCs,[61] or developing RGCs[80] were obtained from the Broad Institute Single Cell Portal as a normalized count matrix, along with the published cluster annotations and UMAP coordinates for each cell. These were loaded into Seurat software[84] for analysis and to generate the gene expression data shown in Figure S1. Data from a separate P5 RGC dataset[60] was accessed via a web-based interface. Cell types within that dataset were identified based on cluster correspondences determined by Shekhar et al.[80]

To assign amacrine clusters as *Unc5c*-positive or -negative (Figure S1E), we took into account overall expression level across all cells in the cluster (average expression > 0) as well as the fraction of expressing cells within the cluster (a minimum of 20% of cells needed to express the gene to call the cluster positive).

Immunohistochemistry
For immunohistochemistry, age-matched mouse eyes of both sexes were collected following euthanasia. Eyes were fixed in 4% paraformaldehyde in PBS for 90 min on ice, then corneas and lenses were removed. To label synapses, lenses were removed prior to fixation and eye cups were fixed in 4% paraformaldehyde in PBS for 45 mins on ice. For retinal cross sections, eye cups were cryoprotected in 30% sucrose and 0.02% sodium azide in PBS, frozen in Tissue Freezing Medium (Triangle Biomedical), cryostat sectioned at 20 μm, and placed on Superfrost Plus slides. Sections were blocked in 3% normal donkey serum in PBS with 0.3% Triton X-100 for 1h at room temperature (RT). For retinal flat mounts, retinas were dissected out of eye cups prior to histology, then blocked for 1-2h at RT. Rat anti-mouse Fc block 1:400 (553142, BD Biosciences) was included in the blocking solution for experiments involving mouse antibodies. The following primary antibodies were used: Guinea pig anti-bassoon 1:500 (141004, Synaptic Systems); goat anti-ChAT 1:400 (AB144P, Millipore); goat anti-FLRT2 1:250 (AF2877 R&D Systems); mouse anti-GAD65 1:1000 (MAB351, EMD Millipore); mouse anti-gephyrin 1:700 (147021, Synaptic Systems); rabbit anti-GFP 1:500 (AB3080P, Millipore); goat anti-GFP 1:500 (ab5450, Abcam); rat anti-Neurofilament-M 1:500 (2H3, Developmental Studies Hybridoma Bank); rabbit anti-Satb1/2 1:500 (2938-1, Epitomics); guinea pig anti-VAChT 1:500 (AB1588, Millipore); mouse anti-Flag 1:1000 (clone M2, F1804, Sigma); rat anti-HA 1:500 (11867423001, Sigma); rabbit anti-mCherry 1:1000 (EMU106, Kerafast). Antibodies were diluted in blocking solution, then applied to retinal sections and incubated overnight at 4°C. For flat mounts, 0.02% sodium azide was included in the primary antibody solution and incubation proceeded for 5-7 d at 4°C on a rocker. Sections were washed three times in PBS and fluorophore-conjugated Jackson ImmunoResearch secondary antibodies were applied at 1:1000 for 2h at RT. The following secondaries were used: Alexa Fluor 488 Donkey Anti-Rabbit [711-545-152]; Cy3 Donkey Anti-Goat [705-165-147]; Cy3 Donkey Anti-Guinea Pig [706-165-148]; Alexa Fluor 647 Donkey Anti-Goat [705-605-147]; Alexa Fluor 647 Donkey Anti-Guinea Pig [706-605-148]; Alexa Fluor 647 Donkey Anti-Mouse [715-605-151]; Alexa Fluor 647 Donkey Anti-Rat [712-605-153]. Slides were washed 3 times in PBS then mounted with Fluoromount G. For wholemounts, retinas were washed several times in PBS over 2-4h at RT on a rocker, then secondary antibodies incubated overnight at 4°C on a rocker. Wholemounts were then washed several times on a rocker at RT over 2 h, mounted on Superfrost slides, coverslipped, and mounted with Fluoromount G.

Western blots and co-immunoprecipitation
Retinas were isolated in dissecting solution: 1X HBSS containing 10mM HEPES and 4mM NaHCO3. Isolated retinas were suspended in lysis buffer containing 100 mM Tris-HCl, pH 8.0, 150 mM NaCl, 1 mM EDTA, and 1%Triton X-100 for 45 min on vertical rotator at 4°C. The sample was vortexed briefly to break up larger pieces of tissue. The sample was sonicated at 20% output of ultrasonicator with pulse ON/OFF cycle for approximately 10 times on ice. Afterward, the lysate was centrifuged at 5,000 rpm for 5 mins at 4°C. The supernatants were transferred into new Eppendorf tubes and centrifugation step was repeated one more time to clear the lysate.

For co-immunoprecipitation (IP) experiments, retina lysates were prepared from a complete litter of P6 CD-1 mice (n = 10 animals). The cleared lysate was split in two equal volumes which were used for experimental (anti-LPHN3) or control (mouse IgG) conditions. For each sample, 5 μg of normal mouse IgG (control) or LPHN3 purified monoclonal antibody was added to the lysate and incubated

with gentle mixing at 4°C for 1 h. Next, 25 μL of Protein A/G beads (Pierce) were added to each sample and incubated overnight at 4°C. The next day, beads were allowed to settle and kept on magnetic apparatus to pull beads away and supernatant was discarded. Dynabeads were washed 3 times with 1X PBS. Lastly, beads were boiled in 10 μL of 4X denaturing sample buffer dye and 10μL of 1XPBS, subjected to SDS-PAGE, and blot transferred onto nitrocellulose membrane. The membranes were incubated with primary antibodies in LI-COR blocking solution overnight at 4°C. Primary antibodies used were: LPHN3[82] (1:500), UNC5C (1:1000) and FLRT2 (1:500). On the next day, the blot was washed 3 times with 1X PBS for 5 min at room temperature. The blot was incubated with LI-COR secondary antibody at dilution of 1:5000 for 1hr RT. The washing step was repeated and subsequently blots were imaged in LI-COR Odyssey imaging system.

For Western blotting of AAV-injected eyes, lysates were prepared at P8 (7 days post-injection) from 2 *Chat^Cre* pups per virus condition (i.e. 4 eyes with flex-tdTomato control and 4 eyes with flex-tdTomato + flex-Unc5c-HA). Sample preparation, blotting, and staining procedures were as described above. Primary antibody was rat anti-hemagglutinin (HA) at 1:500 dilution.

Synapse density in IPL

For quantification of synapses, images were acquired using a Nikon A1 confocal system. Z-stacks (106 μm x 106 μm x 0.33 μm step size; 9-15 steps/z-stack) were acquired using a 60X objective (Plan Apochromat, NA 1.49) with oil immersion and 2X optical zoom. Three independent fields of view (FOV) were used for analysis of ON and OFF sublaminae for each animal (n = 3). All FOV were sampled from a similar retinal eccentricity. Images were deconvolved using Nikon Elements Extended Resolution plugin, then imported into ImageJ. Minor brightness/contrast adjustments were made similarly across all images. Maximum intensity projections of three consecutive 0.33 μm z-sections (for a total z-depth of 1 μm) were used for synapse analysis using the Puncta Analyzer plugin for ImageJ.[85] 3-5 maximum intensity projections were averaged to obtain the number of colocalized puncta per field (dots on graphs). The border between OFF and ON sublaminae was defined based on histologic landmarks.[91] Puncta Analyzer was used to count synapses based on colocalization of presynaptic and postsynaptic markers as previously described.[85,91] In brief, the projected images were divided into individual channels (presynaptic and postsynaptic markers); background was subtracted for each channel (rolling ball radius = 50); thresholds were adjusted manually to detect individual puncta while minimizing background; and puncta smaller than 4 pixels were filtered out. For all conditions, n = 3 animals per genotype, with 3 FOV per animal. Single slices of the z-stacks were chosen for presentation of representative images. Standard error was calculated from 9 FOV from 3 animals per genotype.

Synapse identification on ooDSGC dendrites

To visualize the distribution of synaptic puncta along dendrites of GFP-labeled ooDSGCs, we utilized a semi-automated method of synapse identification.[51] Images of of synaptic puncta were acquired at a voxel size of 0.104 x 0.104 x 3 μm, deconvolved using Nikon Elements software, and then converted to 8-bit in ImageJ. Using the Simple Neurite Tracer plugin for ImageJ,[92] we generated a 3D mask of the GFP channel and then used a MATLAB application Object Finder[51] to identify synaptic puncta within the mask. Object Finder was run with the following settings to segment bassoon and gephyrin puncta: Expected size range = 0.2-5.0 μm; algorithm = iterative thresholding; connectivity = 6; noise estimation = standard deviation; watershed, block search, local noise = true; minimum object intensity = 2x above noise; exclude if single z plane = true. For calling synapses, the minimum overlap between segmented bassoon and gephyrin voxels was set to 50%.

Analysis of laminar targeting phenotypes

Retinal cross sections (20 μm) were prepared from P6, P10, or P15 animals. Each section was collected sequentially on a series of microscope slides, such that each slide contained an evenly-spaced series of sections (200 μm section interval). For counting of laminar errors, 2-3 sections per animal were chosen for analysis. The chosen sections were separated by at least 100 μm – larger than most of the observed errors – so as to minimize the chances of counting the same error in multiple sections. The chosen sections were also limited to the most central portion of the tissue block, such that sections were as perpendicular as possible to the IPL layers. This selection was crucial to ensure that tissue curvature did not influence scoring of IPL sublaminar position.

Each chosen section was manually inspected for laminar targeting errors using fluorescence microscopy, and all instances of mistargeted dendrites within the section were counted. "Starburst errors" were defined as VAChT+ arbors ramifying above or below the main S2 or S4 VAChT bands. "ooDSGC errors" were defined as GFP+ arbors that resided in ectopic sublayers and were uncoupled from the starburst scaffold. (When ooDSGC dendrites followed starburst arbors into an ectopic sublayer, this was only counted as a starburst error). Notably, we could not distinguish the number of different cells contributing dendrites to these mistargeted laminar fascicles, so each instance was counted only as a single error. If an error was seen at the same retinal location in multiple sections, it was only counted once, to rule out the possibility that the same mistargeted dendrites might extend across the 100 μm section distance and be counted twice. Confocal z-stacks (0.3-1.0 μm z step) were taken for each region of interest containing an error. While single confocal slices (or a Z-projection of a subset of the stack) are shown here for illustration purposes, each error was verified by examining the full confocal stack. For each section analyzed, the end-to-end length of the IPL was measured in FIJI using the Freehand Line tool. This length was then used to express the number of targeting errors observed in each section as errors per millimeter.

Satb1 co-labeling[29] was used to confirm that the vast majority Hb9-GFP+ cells are *bona fide* ooDSGCs at the ages used in this study (Figures S4A and S4B). When Satb1-negative GFP cells were observed, they were always located in the far peripheral retina. Therefore, for Hb9-ooDSGC analysis, the two most peripheral 60X fields of view (FOVs) were not used because these FOVs occasionally include ganglion cells that are not ooDSGCs (Figures S4A and S4B). Phenotype graphs show averaged data from at least 2

sections per animal. Control groups in these graphs show pooled wild-type littermate data from *Flrt2* and *Unc5c* strains, as these different controls did not show phenotypic differences.

Mistargeted arbors were represented graphically by generating fluorescence profile plots through the IPL using FIJI. Raw data were exported to Excel, and for each channel the background signal was subtracted and resulting values were normalized to signal maxima. Images were median filtered (radius = 0.5 pixels) to remove background noise from photomultiplier tube.

For en-face imaging of ooDSGC laminar errors in retinal wholemounts, confocal z-stacks were acquired through the depth of the IPL at a z resolution of 0.4 - 0.6 μm. Representative images shown in Figure 2M depict a maximum projection of a small number of z-slices (encompassing approximately 1 μm of z distance), acquired at the level of the INL/IPL border. This region does not normally contain ooDSGC dendrites in wild-type retina.

Two-photon guided morphological reconstructions

Isolated whole retinas from adult (∼P40) mice were micro-cut at the dorsal and ventral halves to allow flattening, with dorsal and ventral mounted over a 1–2 mm^2 hole in nitrocellulose filter paper (Millipore) with the photoreceptor layer side down and stored in oxygenated Ames' media (maximum 10 h).

Identification, dye loading and imaging of GFP$^+$ ooDSGCs was performed as described previously.[93] In brief, GFP$^+$ cells were identified using a custom-modified two-photon microscope (Fluoview 300; Olympus America) tuned to 920 nm to minimize activation and bleaching of photoreceptors. The inner limiting membrane above the targeted cell was dissected using a glass electrode. Cell attached voltage clamp recordings were performed with a new glass electrode (4-5 MΩ) filled with internal solution containing the following (in mM): 110 CsMeSO4, 2.8 NaCl, 20 HEPES, 4 EGTA, 5 TEA-Cl, 4 Mg-ATP, 0.3 Na$_3$GTP, 10 Na$_2$Phosphocreatine, QX-Cl and Alexa-594 Hydrazide dye (pH = 7.2 with CsOH, osmolarity = 290, ECl$^-$ = -60 mV). Signals were acquired using Clampex 10.4 recording software and a Multiclamp 700A amplifier (Molecular Devices), sampled at 10 kHz, and low pass filtered at 6 kHz. The Alexa dye freely diffused into the ooDSGC cytoplasm after obtaining a giga ohm (1GΩ) seal and breaking into the cell membrane. Cells were imaged for electrode positioning using two photon excitation at 800 nm. At this wavelength, GFP is not efficiently excited thereby preserving fluorescence for anatomical imaging.

Next, morphological reconstruction and dendritic segmentation were performed as described previously.[93] Briefly, 480 x 480 μm Image stacks were acquired at z intervals of 1.0 μm and resampled fifteen times for each stack using a 20X objective (Olympus LUMPlanFl/IR 2x digital zoom, 1.0 NA) and 30kHz resonance scanning mirrors covering the entire dendritic fields of the ooDSGCs. Image stacks of ooDSGCs were then imported to FIJI and a custom macro was used to segment ON and OFF dendrites based on their lamination depth in the inner plexiform layer (ON layer 10-30 μm, OFF layer 35-55 μm depth). Following ON and OFF dendritic segmentation, we used the Simple Neurite Tracer plugin on FIJI to skeletonize and then binarize the ON and OFF dendritic segments for morphological analyses.

UNC5C gain of function

For AAV production we generated a ITR-CMV-*flex-Unc5cHA-WPRE-SV40pA-ITR* construct. A cDNA encoding *Unc5c*[11] was tagged at the 3' end with a 3xHA epitope tag and cloned behind a mini-CMV promoter containing the MVM small intron. Cre-dependence of expression was conferred using the flex-switch strategy.[94] AAV particles of serotype PHP.eB were produced from this plasmid by the Duke Viral Vector Core. CAG-flex-tdTomato viral particles (gift of Edward Boyden) was purchased from Addgene (Addgene viral prep #28306-PHPeB).

For AAV administration, heterozygous *Chat*^{Cre} P1-2 neonatal mice were anesthetized on ice until unresponsive to toe pinch. Eyelids were cleaned with an ethanol wipe, then a guide hole was punctured at the outer edge of the ora serrata using a 30G needle. A Hamilton syringe was used to inject 0.5-0.75 ul of virus and 1:10 FastGreen was included to visualize injection success. Left eyes were injected with a 5:1 mixture of experimental virus (AAV-flex-Unc5c-HA) and tdTomato reporter virus (AAV-flex-tdTomato); right eyes were injected with the tdTomato reporter virus alone as control. Mice were recovered on a heated pad until they regained pinkness and light aversion. Pups were returned to their home cage with mother after recovery. After 4 weeks, mice were sacrificed and eyes were harvested for histology. Anti-HA staining was performed on each retina to confirm UNC5C protein expression. To confirm the timing of UNC5C-HA expression, a cohort of animals was also collected 1 week post-injection and was subjected to anti-HA immunostaining and Western blotting (Figure S7B).

For phenotypic analysis, an evenly-spaced series of 20 μm cryosections was prepared and selected for analysis as described in "Analysis of laminar targeting phenotypes" above. To ensure accuracy of laminar scoring results, only sections through the most central portion of the retina, perpendicular to the IPL sublayers, were selected for analysis. In each analyzed section, retinal regions containing virally transduced cells were identified using tdTomato expression. Laminar errors were then scored within these regions.

QUANTIFICATION AND STATISTICAL ANALYSIS

Statistical tests were performed using GraphPad Prism software. Non-parametric tests were used in many cases, because large numbers of "0" values (typically in the control condition) led to non-normal data distributions. Sample sizes, statistical tests used, and P-values are given in figure legends and graphs where applicable; otherwise they are given in results.